Early Eocene A-type (ferroan) rhyolites in southwestern Tibet: A far-field tectonic effect of the India–Eurasia collision

Chenwei Li, Zhijun Li, Min Zeng & Robert J. Stern

View supplementary material

Published online: 01 Sep 2022.

Submit your article to this journal

Article views: 200

View related articles

View Crossmark data

Citing articles: 1 View citing articles

Taylor & Francis
Taylor & Francis Group

Check for updates

Early Eocene A-type (ferroan) rhyolites in southwestern Tibet: A far-field tectonic effect of the India–Eurasia collision

Chenwei Li [a], Zhijun Li[a], Min Zeng[b] and Robert J. Stern[c]

[a]College of Earth Sciences, Chengdu University of Technology, Chengdu, 610059, China; [b]School of Earth Sciences, Yunnan University, Kunming, 650500, China; [c]Geosciences Department, University of Texas at Dallas, Richardson, TX 75080, USA

ABSTRACT

Eocene igneous rocks along the Gangdese belt in southern Tibetan Plateau are important for understanding the India–Eurasia collision and Tibetan Plateau uplift. These magmatic rocks are widely considered to be related to roll-back or break-off of the Neotethyan slab during northward subduction. However, Eocene rhyolites in the northwestern Gangdese belt (SW Qiangtang margin) do not fit either the rollback or breakoff models. This paper investigates these Early Eocene lavas and compares them with contemporaneous igneous rocks along the Gangdese belt via detailed field observations, petrology, zircon geochronology, zircon Lu–Hf isotopes and whole-rock geochemistry. These felsic lavas form large outcrops in western Tibet and have two zircon U–Pb ages of 54.71 ± 0.14 Ma and 54.74 ± 0.27 Ma. They have high SiO_2 and alkali contents, FeO*/MgO, and Ga/Al ratios as well as strongly negative Eu anomalies and slightly positive zircon $\varepsilon Hf(t)$ values (+2.5 to +4.4). Both Ti-in-zircon and Zr saturation thermometers confirm high magmatic temperatures (~900°C). They are ferroan, A-type rhyolites. Furthermore, the distinctive low $\varepsilon Hf(t)$ values imply that these rhyolites are likely partial melting products of the southwestern Qiangtang Terrane. The lithosphere in this region undergone long-term shortening and thickening since 80–95 Ma. Pre-thickened lithosphere may be a prerequisite for the Early Eocene delamination, and the simultaneous inducement is a far-field tectonic effect from the India–Eurasia collision. We suggest that: (1) India collided with Eurasia before 55 Ma and triggered delamination to form the Shiquanhe A-type rhyolites on the southwestern Qiangtang margin thereafter; and (2) tectonic stresses related to India–Eurasia collision during the Eocene were transmitted efficiently over large distances.
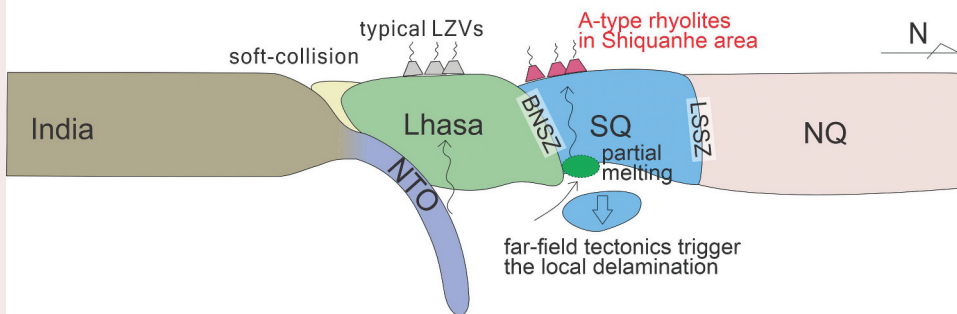
1. Introduction

Widespread Eocene igneous rocks across the Tibetan Plateau exhibit systematic variations in space and time that are probably related to both northward Neotethys subduction and India–Eurasia collision (Figure 1B; Table S1; Ji *et al.* 2012; Lee *et al.* 2009; Wang *et al.* 2010; Wang *et al.* 2015). Studies increasingly suggest that these magmatic contributions are also important for Tibetan

Plateau crustal thickening and uplift (Mo *et al.* 2007; Lee *et al.* 2009; Wang *et al.* 2010, 2014a, 2015; Dokuz 2011; Ji *et al.* 2012). Eocene magmatism is important for deciphering the tectonic history of the Tibetan Plateau, which produced a series of magmatic rocks consisting of the Linzizong volcanic succession (LZVs) along the Gangdese belt and Eocene adakitic rocks (EARs) of the Qiangtang Terrane (Figure 1B; Chapman *et al.* 2018; Ji
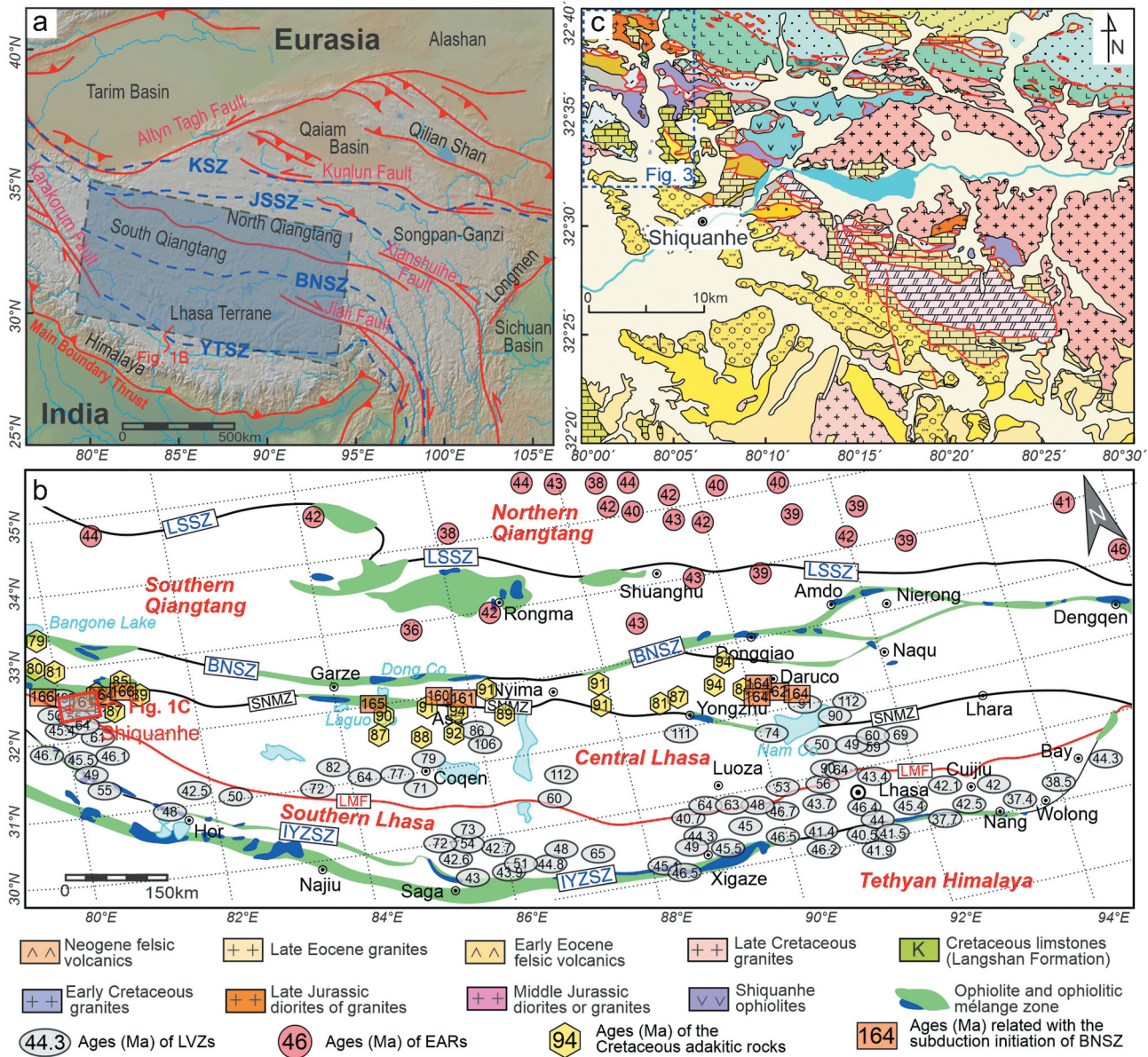
Figure 1. (A and B) Simplified geological and tectonic maps of the Tibetan Plateau (after Pan *et al.* 2004; Zhu *et al.* 2013). KSZ, Kunlun Suture Zone; JSSZ, Jinsha Suture Zone; BNSZ, Bangong-Nujiang Suture Zone; YTSZ, Yarlung Tsangpo Suture Zone. (C) Geological map of the Shiquanhe area. The red star marks the location of the Shiquanhe rhyolites.

et al. 2009; Wang *et al.* 2015, Wang *et al.* 2015a; Zeng *et al.* 2020). The LZVs distributed throughout the Gangdese belt contain several magmatic units dating to 64.5–40.8 Ma, which are widely accepted as products of Neotethyan oceanic slab rollback, early stages of slab break-off, and India–Eurasia collision, respectively (Haschke *et al.* 2002; Chung *et al.* 2005; Lee *et al.* 2009; Dokuz 2011; Zhang *et al.* 2012; Wang *et al.* 2015a). In addition, EARs represent the extensive Eocene volcanic rocks with minor intrusive equivalents that formed abruptly after a magmatic lull since the Early Cretaceous in the Qiangtang Terrane, and provide

prime access to the deep processes responsible for the formation of the protoplateau (Zeng *et al.* 2020).

Here, we document Late Cretaceous to Late Eocene igneous rocks along the southern Qiangtang margin and the Gangdese magmatic belt (Figure 1). The results confirm the southward migration of arc magmatic rocks from the Late Cretaceous to the Paleocene and magmatic 'flare-ups' related to Early Eocene slab break-off (Ji *et al.* 2009; Lee *et al.* 2009; Wang *et al.* 2015; Huang *et al.* 2017; Chung *et al.* 2005, Figure 1B and Figure 2). This voluminous Eocene magmatism is characterized by extensive

Figure 2. (A) Histogram of zircon U-Pb ages for igneous rocks along the Gangdese belt. (B) Plot of ages *vs*. distance from the YTSZ.
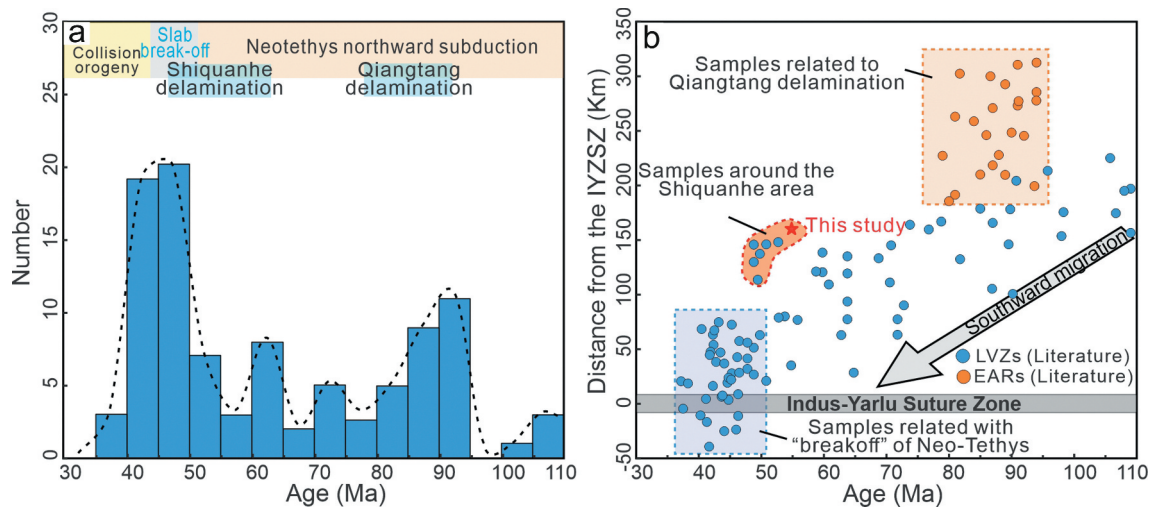
I-type calc-alkaline to high-K calc-alkaline magmatic rocks. Most of these rocks have been studied in the eastern Gangdese belt (east of ~89°E); however, less work has been done to the west (Wang *et al*. 2015). Therefore, we performed whole-rock geochemistry and zircon dating on new samples from the western Tibetan Plateau, the Shiquanhe area, to determine their origin. However, Eocene rhyolites around the Shiquanhe area differ from both the LZVs and the EARs. The results show that Shiquanhe rhyolites have distinctive A-type geochemistry (Whalen *et al*. 1987; Eby 1992; Zhang *et al*. 2007), indicating that there was a source of dehydrated, reasonably salic crust, and a source of high heat sufficient to partially melt this crust (Whalen *et al*. 1987; Bonin 2007). Based on the zircon Hf isotopes, we think that lower crustal delamination and asthenospheric mantle upwelling partially melted the SW Qiangtang lithosphere. Early Eocene delamination was likely limited to the SW Qiangtang margin. We suggest that this local delamination was due to the pre-thickened lithosphere formed since the initial Lhasa–Qiangtang terrane collision during the Early Cretaceous (Kapp and DeCelles 2019; Lai *et al*. 2019). Next, the initiation of India–Eurasia collision may have triggered lithospheric delamination beneath the Shiquanhe area as a far-field tectonic effect. We prefer this model to explain Eocene Shiquanhe A-type rhyolites. More importantly, we provide a new example of far-field tectonic effects that are transmitted efficiently over large distance on the India–Eurasia collision area, which is similar to the Arabia-Eurasia collision area (Albino *et al*., 2014; Cavazza *et al*. 2017; Gusmeo *et al*. 2021).

2. Geological setting and sample description

The Himalayan–Tibetan orogen consists of several continental blocks with Gondwana affinity (e.g. Himalayan sequences, Lhasa Terrane and Qiangtang Terrane, and Songpan–Ganze Complex, from south to north; Zhu *et al*. 2013; Metcalfe 2013, Figure 1A). These blocks progressively accreted to form three sutures: the Yarlung Tsangpo Suture Zone (YTSZ), the Bangong–Nujiang Suture Zone (BNSZ), and the Jinsha River Suture Zone (JSSZ) from south to north (Zhu *et al*. 2013; Figure 1A). The JSSZ was produced by closing the Paleo-Tethys Ocean and is represented by the Jinshajiang ophiolitic belt (Wang *et al*. 2000). The BNSZ in central Tibet is a remnant of the Bangong–Nujiang Tethys Ocean (BNO; also known as the Meso-Tethys) and separates the Lhasa Terrane and Qiangtang Terrane along two nearly parallel discontinuous ophiolite belts extending more than 2000 km (Xu *et al*. 2014; Li *et al*. 2020, 2020a, 2021). The YTSZ marks the closure of the Neotethyan Ocean and lies south of an east-west-trending Andean arc-type calc-alkaline magmatic zone (known as the Gangdese Magmatic Belt) in the Lhasa Terrane (Figure 1A and 1B; Lee *et al*. 2012; Zhu *et al*. 2011; Hu and Stern 2020).

The Lhasa Terrane has been subdivided into three subterranes from south to north (Zhu *et al*. 2011; Metcalfe 2013). Both the Central Lhasa and South Lhasa Subterranes consist of Precambrian crystalline basement covered by Paleozoic and Mesozoic metasedimentary and metavolcanic rocks (Pan *et al*. 2004; Zhu *et al*. 2009; Lin *et al*. 2013). The Nyainqêntanglha Group of the Central Lhasa Subterrane has been interpreted as Neoproterozoic basement, which consists mainly of amphibolite facies metamorphic rocks with ages of 690–787 Ma (Pan *et al*. 2004; Zhu *et al*. 2013).

Orthogneisses of the Nyingchi Group indicate 550–496 Ma as the age of the South Lhasa Subterrane basement (Dong *et al.* 2010), although the oldest magmatic cores of zircons in the eastern segment of the South Lhasa Subterrane yield protolith ages of 1784 ± 25 Ma and 1782 ± 31 Ma (Lin *et al.* 2013). However, it should be noted that Proterozoic zircons in southern Lhasa Terrane are only found in the easternmost part of southern Lhasa Terrane (Lin *et al.* 2013). On the other hand, the North Lhasa Subterrane is dominated by juvenile crust formed by accretion accompanying subduction along the BNO (Zhu *et al.* 2011, 2013). BNO subduction formed a series of Cretaceous volcanic rocks (andesite to rhyolite varieties) and granitoids that show positive zircon εHf(t) (Zhu *et al.* 2011). The oldest intrusive rocks in the North Lhasa Subterrane are the Early Jurassic (185–181 Ma) Shiquanhe granodiorites (Li *et al.* 2021aa). In addition, based on zircon Hf isotope mapping, Hou *et al.* (2015) suggested that the Central Lhasa Subterrane is a long-standing Precambrian microcontinent with local reworking crust, and that the two surrounding juvenile Phanerozoic crustal blocks, the North Lhasa and South Lhasa Subterranes, have significant mantle contributions to constituent magmatic rocks.

Although increasing numbers of studies have been carried out on the Lhasa Terrane, the times of initial continental rifting and final subduction-to-collision are controversial (Yin and Harrison 2000; Wang *et al.* 2019, 2020; Chen *et al.* 2020). Most previous studies proposed that the Lhasa Terrane rifted from Gondwana during the late Carboniferous–early Permian during Neotethyan Ocean or Sumdo Tethys opening (Zhu *et al.* 2013; Zeng *et al.* 2019) and then accreted to the Qiangtang Terrane during the Cretaceous (Yin and Harrison 2000; Hu *et al.* 2016; Zeng *et al.* 2019; Chen *et al.* 2020). Considering the widespread arc-related magmatism in the Qiangtang Terrane and the absence of coeval arc igneous rocks in the Lhasa Terrane, northward subduction of the BNO is accepted to have resulted in collision between the Lhasa Terrane and Qiangtang Terrane (Kapp and DeCelles 2019; Li *et al.* 2020a). Lithospheric delamination that developed as the Lhasa–Qiangtang collision progressed is proposed to have caused Late Cretaceous adakitic magmatism (80–95 Ma) within the Lhasa–Qiangtang collision zone (Yi *et al.* 2018; Sun *et al.* 2020). In the south, the Neotethys also subducted northward under the Lhasa block, forming the well-known Gangdese magmatic belt, which spans the length of the Himalayas with a width of 100–200 km (Mo *et al.* 2008; Lee *et al.* 2012; Ding *et al.* 2014). The Gangdese magmatic belt is considered the product of both northward subduction of the Neotethyan Ocean and the India–Eurasia collision (Mo *et al.* 2008; Zhu *et al.* 2019). Its

evolution can be divided into three stages: Mesozoic (Late Triassic–Cretaceous), Paleocene–Eocene, and Oligocene–Miocene (Ji *et al.* 2009). During the first stage, Andean-type subduction of the Neotethyan Ocean produced typical arc-related calc-alkaline magmas. Next, India–Eurasia collision led to the negative buoyancy of the India continental mass in the collision zone. This process may have led to lithospheric necking, as a result, roll-back and break-off of the Neotethyan oceanic slab formed calc-alkaline to shoshonitic magma suites known as the LZVs (Chung *et al.* 2005; Ji *et al.* 2009; Lee *et al.* 2012) and other intrusive rocks, such as gabbro and appinites (e.g. Huang *et al.* 2017, 2019). In the last stage, India–Eurasia collision created adakitic rocks and ultrapotassic-potassic rocks, which were caused by the convective removal of lithospheric roots (Chung *et al.* 2005; Guo *et al.* 2007).

Samples for this study were obtained mainly from newly discovered volcanic rocks along the southern BNSZ margin around Shiquanhe County, western Tibetan Plateau (Figures 1C and 3). Based on the division of Zhu *et al.* (2013), the Shiquanhe area lies in the North Lhasa Subterrane and belongs to the northwestern segment of the Gangdese belt. However, the following considerations indicate that Shiquanhe rhyolites and contemporaneous magmatic rocks in this area differ from the LZVs: (1) Shiquanhe rhyolites are located on the north side of the southern boundary of the BNSZ, while typical LZVs are distributed more than 100 km to the south of this boundary (Li *et al.* 2020), Figure 1B. (2) Shiquanhe rhyolites are located on the southern margin of the Shiquanhe accretionary complex (Figure 3; Figure 4F, G). (3) The geochemical characteristics of Shiquanhe rhyolites are distinct from those of typical LZVs, as presented below.

We measured a 20 km structural/stratigraphic section along a north–south traverse across the Shiquanhe ophiolitic mélange belt north of Shiquanhe County (Figures 1C and 3). In this section, a series of northward-dipping thrust faults surrounding mélanges were identified. Most of these mélanges exhibit chaotic block-in-matrix fabric (Figure 3), similar to a subduction channel mélange (Draut and Clift 2013). In the northern part of the section, broken formation is characterized by a block-in-matrix fabric in which part of the same coherent stratigraphic unit can be recognized without 'exotic' blocks, which present a kind of typical mélange related to subduction (Festa *et al.* 2010, 2019). These mélanges were formed by northward subduction of the Bangong Meso-Tethys, which terminated after the Lhasa–Qiangtang collision in the Late Cretaceous (Chen *et al.* 2018; Li *et al.* 2020). The Shiquanhe rhyolites are located along the southern margin of the above mélange zone
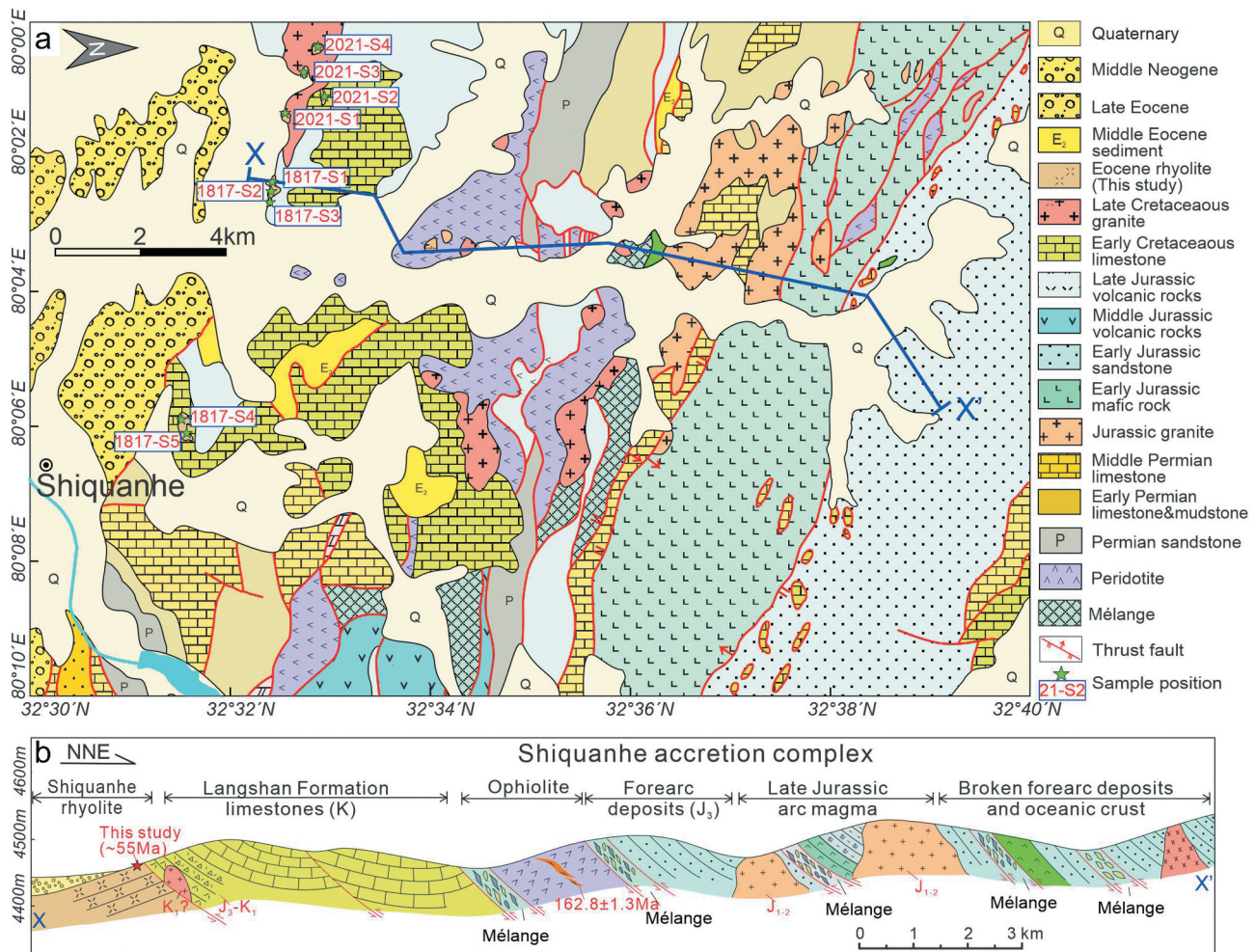
Figure 3. (A) Cross-section of the accretionary prism in the Shiquanhe area. (B) Large-scale geological map around the Shiquanhe area and detailed sampling locations.

(Figure 3). The outcrops of rhyolites are generally discontinuous with thicknesses of ~20 m to ~40 m, are purple–gray to gray, and contain well-preserved fluxion structures with elongated muscle tracks (Figures 4F-I). Rhyolites are covered by Cretaceous limestones beneath a north-dipping thrust fault (Figure 3 and Figure 4G). These field occurrences and the structural aspects of the Shiquanhe rhyolites indicate that the extrusive's location is along the southern boundary of the BNSZ (Figures 1C, 3 and 4F-I). To ensure reliable and representative data, we sampled this unit in the field as extensively as possible, covering an area with a radius of approximately 10 kilometers. The sample locations are shown in Figure 3.

In thin section, Shiquanhe rhyolites are porphyritic with quartz and feldspar phenocrysts and have groundmasses of feldspar, biotite, quartz, apatite, and zircon. Quartz phenocrysts are uniaxial positive (+ve) crystals and have euhedral hexagonal shapes; thus, they are high-temperature β-type quartz. Feldspar phenocrysts are euhedral and biaxial negative (-ve) crystals with

simple twins, indicating that they are alkali feldspars (Figure 4A-E).

3. Analytical methods

3.1. Zircon geochronology (U–Pb isotopes, Lu–Hf isotopes, and trace elements)

Zircons were separated from crushed host rocks using heavy liquid and magnetic techniques and then hand-picked under a binocular microscope. Zircon grains were randomly mounted in epoxy resin and polished to approximately half of their thickness. Subsequent analyses were acquired on the outermost rim of each zircon with the aid of cathodoluminescence (CL) images and transmitted and reflected light images (Figure 5). All zircon analyses were performed at the Wuhan Sample Solution Analytical Technology Co., Ltd., China, following procedures in Li *et al*. (2010) and Zong *et al*. (2017). Laser ablation inductively coupled plasma–mass spectrometry (LA-ICP–MS) was used to analyze U–Pb
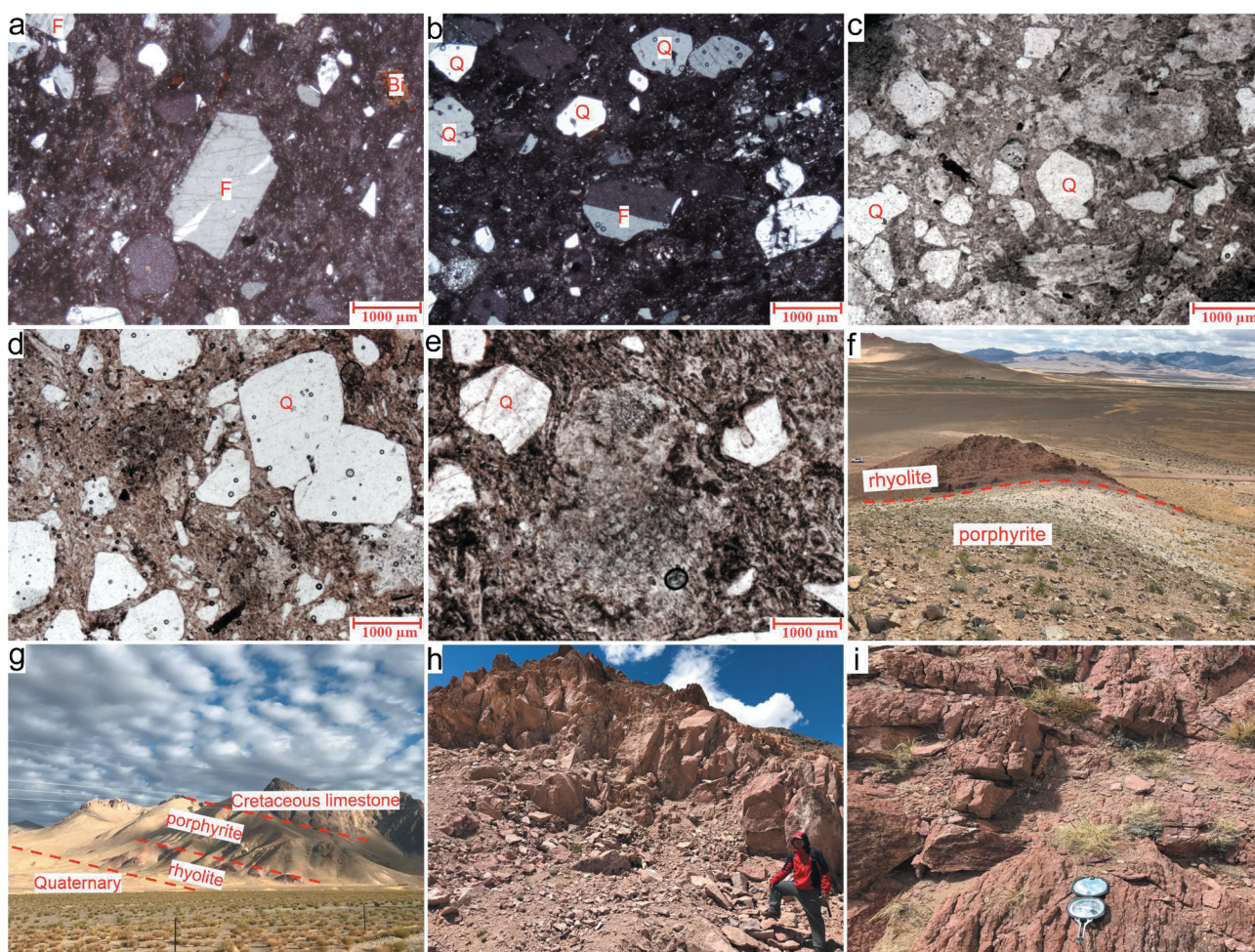
Figure 4. (A-E) Representative photomicrographs. Shiquanhe rhyolites are porphyritic with quartz and feldspar phenocrysts with groundmasses of feldspar, biotite, quartz, apatite, and zircon. Quartz phenocrysts are euhedral hexagonal β-type quartz. Feldspar phenocrysts are euhedral with simple twins. (F-I) Photographs of Shiquanhe rhyolites in the field.

isotopes and trace elements. Analyses were performed using a GeoLasPro laser ablation system that consisted of a COMPexPro 102 ArF excimer laser (wavelength of 193 nm and maximum energy of 200 mJ) and a MicroLas optical system. Helium was the carrier gas. Argon was used as the makeup gas and mixed with the carrier gas via a T-connector before entering the ICP. Dating was conducted with an Agilent 7500e ICP–MS equipped with a 32 μm laser spot diameter. U, Th, and Pb concentrations were calibrated using Zircon 91,500 as the external standard. The trace element concentrations of zircons were calibrated using NIST 610 glass as the external standard. Each analysis incorporated a background acquisition of approximately 20–30 s followed by 50s of sample data acquisition. The results were calculated with ICPMSDataCal v.11 (Liu *et al.* 2008), and concordia diagrams and weighted mean calculations were completed with Isoplot 4.0 (Ludwig 2003). Analyses with > 10% discordance were excluded to ensure the accuracy of every single zircon, and ^{206}Pb/^{238}U ages are reported.

In situ zircon Lu–Hf isotopes were analyzed using a Neptune Plus multicollector MC-ICP-MS in combination with a GeoLas HD excimer ArF laser ablation system. Helium was used to carry gas into the ablation cell, and argon was used as the makeup gas after the ablation cell. Laser spots were 44 μm in diameter and located on top of LA-ICP-MS spots. The laser ablation energy density was ~7.0 J/cm^2. Each measurement consisted of 20s of background signal acquisition and 50s of ablation signal acquisition. Additional details on the operating conditions and analytical methods are given in Hu *et al.* (2012). Off-line selection, integration of analyte signals, and mass bias calibrations were performed with ICPMSDataCal v.11 (Liu *et al.* 2010).

3.2. Major and trace element geochemistry

The nine least altered granite samples were analyzed in the Mineral Laboratory of ALS Co., Ltd. (Guangzhou, China). Samples were rinsed with water, dried, jaw-
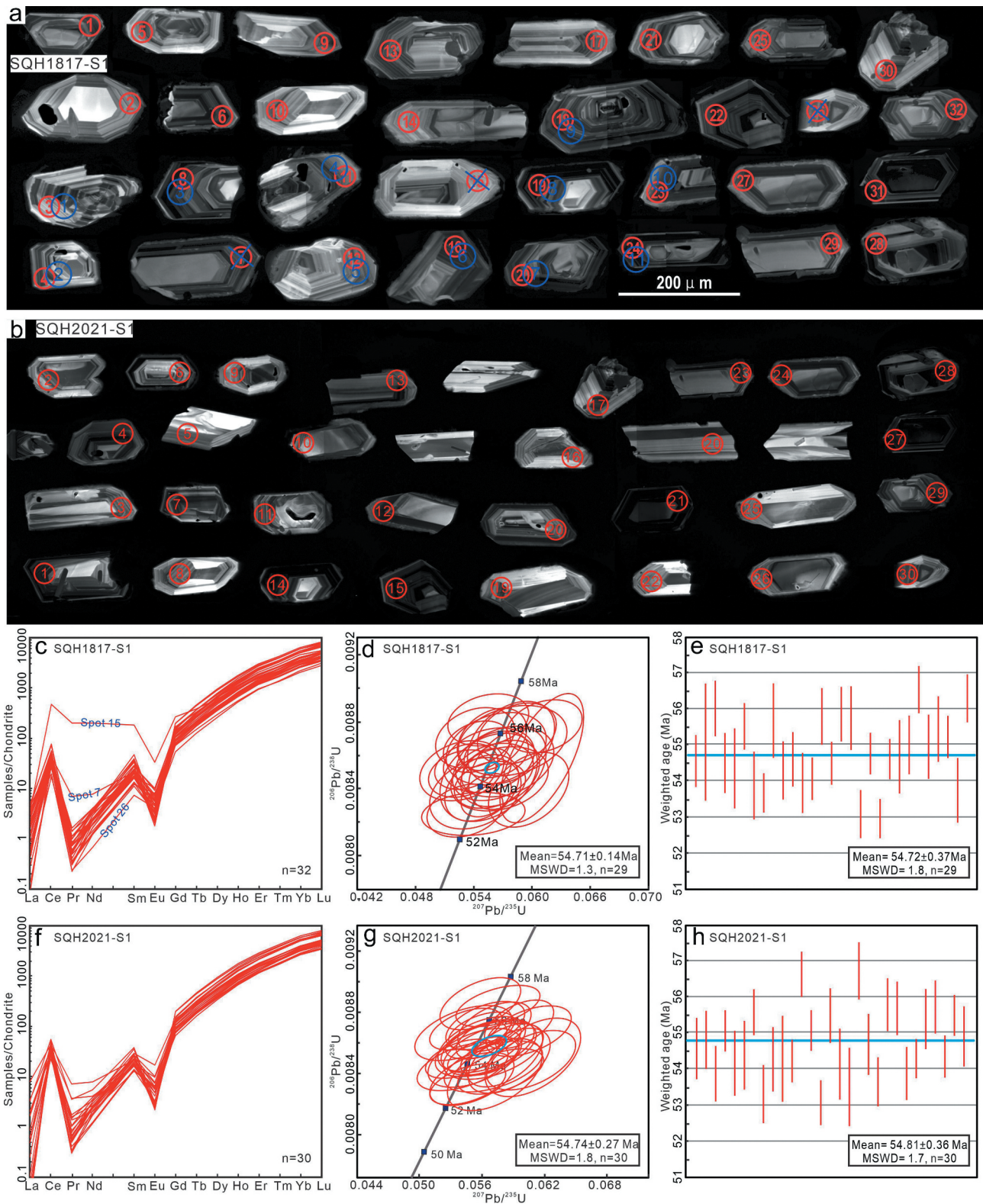
Figure 5. (A) Cathodoluminescence (CL) images of zircons from the Shiquanhe rhyolites. (B) Chondrite-normalized diagrams for zircons from the Shiquanhe rhyolites. (C) Concordia plots of U-Pb zircon data for zircons from the Shiquanhe rhyolites. (D) U-Pb zircon weighted age diagrams of Shiquanhe rhyolites.

crushed, and then pulverized into 200 mesh powders using an agate mortar. Loss on ignition (LOI) was calculated by heating sample powders to 1000°C for three hours. Major elements were determined by X-ray fluorescence (XRF) spectrometry (PW2424, Malvern Panalytical, Almelo, Holland). Analytical uncertainties were generally within 5%. Trace elements were analyzed by ICP–MS (Agilent 7900) after acid digestion in a Teflon bomb. The analytical uncertainty was better than 10%.

4. Results

4.1. Zircon U–Pb geochronology, trace elements and Lu–Hf isotopes

The analytical results for 62 test spots on two samples are listed in Table S2 and shown in Figure 5. These zircons are euhedral and stubby with clear oscillatory zones in CL images, and most are 140–200 μm long with axial ratios of 2:1–3:1 (Figure 5A). Moreover, zircons exhibit elevated U/Th ratios (1.48 ± 0.23), U/Yb ratios (1.09 ± 0.30), heavy rare earth element (HREE) enrichment, strong positive Ce anomalies (Ce/Ce* = 47.3 ± 38.3), and negative Eu

anomalies (Eu/Eu* = 0.10 ± 0.06) (Figure 5B). These characteristics are consistent with their magmatic origin (Hoskin and Schaltegger 2003; Grimes et al. 2007). Two samples yield concordia ages of 54.71 ± 0.14 Ma (mean square weighted deviation, MSWD = 1.3) and 54.74 ± 0.27 Ma (MSWD = 1.7) (Figure 5C). These ages agree with $^{206}Pb/^{238}U$ weighted average ages of 54.72 ± 0.37 Ma (MSWD = 1.8) and 54.81 ± 0.36 Ma (MSWD = 0.17) (Figure 5D). The uncertainties for these ages are given as 1σ errors at the 95% confidence level.

Thirteen test spots on zircons yield Lu–Hf isotope compositions shown in Table S3 and Figure 6. The initial $^{176}Hf/^{177}Hf$ and $\varepsilon_{Hf}(t)$ values and T_{DM}^{C} ages were calculated using the mean weighted zircon $^{206}Pb/^{238}U$ ages. These zircons have low $^{176}Lu/^{177}Hf$ ratios (0.00173–0.00224), indicating that negligible radiogenic ^{176}Hf accumulated after crystallization. The results exhibit relatively homogeneous Hf isotope compositions, with $^{176}Hf/^{177}Hf$ ratios from 0.282811 to 0.282864 and $\varepsilon_{Hf}(t)$ values from +2.5 to +4.4, corresponding to T_{DM}^{C} ages from 747 to 853 Ma. The $\varepsilon_{Hf}(t)$ vs. The zircon U–Pb age diagram shows Hf isotope variations (Figure 6).

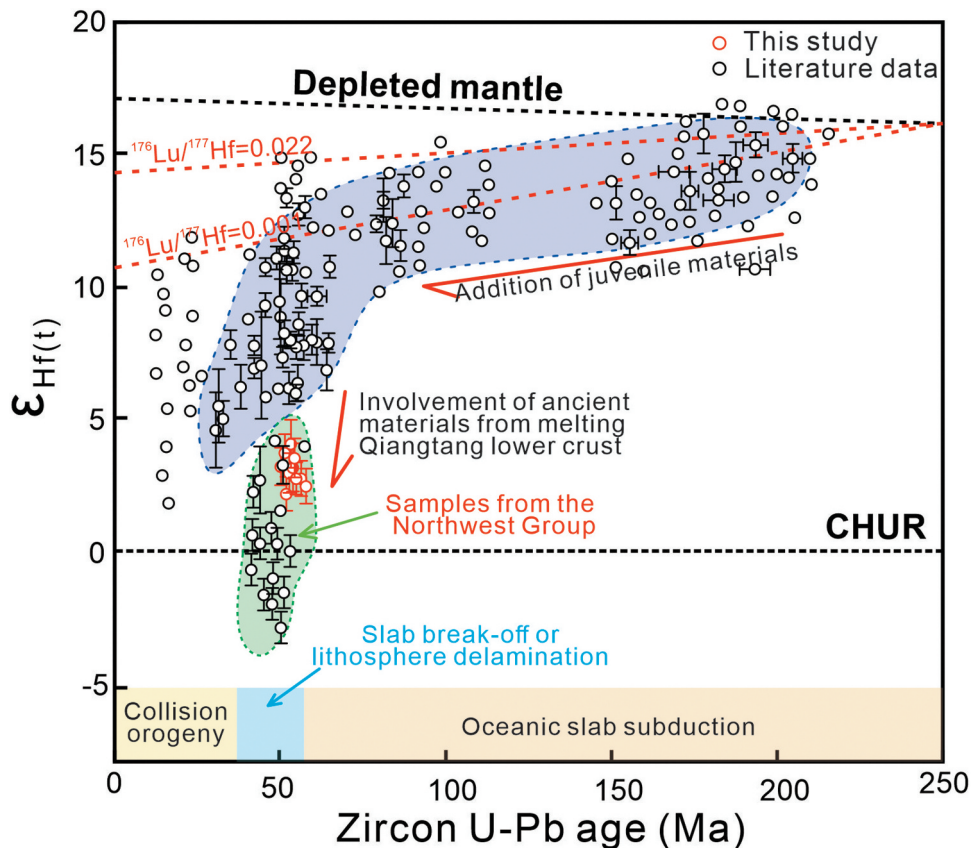**Figure 6.** Binary plot of $\varepsilon_{Hf}(t)$ values *vs.* ages of the Gangdese batholith. Literature data are from Wang *et al.* (2015), Wen et al. (2008), Dong (2008), Ji *et al.* (2009), (2012), Ji (2010), Huang et al. (2010), Zhu *et al.* (2011), Guan et al. (2012), Cong et al. (2012), Jia (2014), Chu et al. (2006), Zhang *et al.* (2007), Schaltegger et al. (2002), Heuberger et al. (2007).
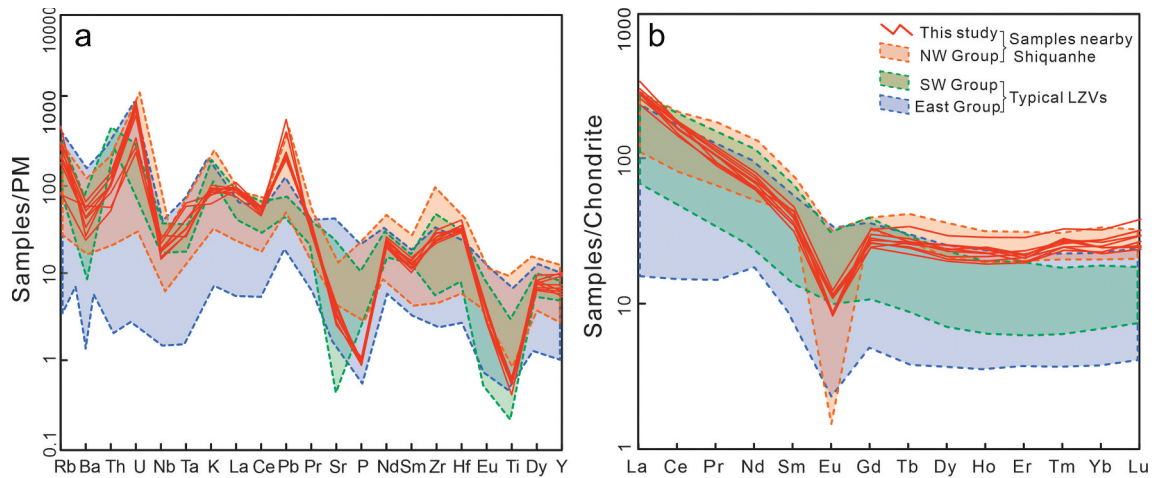
Figure 7. (A) Primitive mantle-normalized (Samples/PM) trace element patterns. (B) Chondrite-normalized rare earth element patterns (from Sun and Mcdonough 1989).

4.2. Major and trace element geochemistry

The nine least altered samples were selected from different locations around Shiquanhe County for whole-rock major and trace element analyses, and the results are listed in Table S4. The loss on ignition of all samples is less than 1.9 $wt.\%$, suggesting modest alteration. The samples have high SiO_2 (70.1–73.1 $wt.\%$) and K_2O (5.1–6.6 $wt.\%$) contents, moderate contents of Al_2O_3 (11.1–13.1 $wt.\%$) and Na_2O (3.2–4.4 $wt.\%$), and low contents of MgO (0.2–0.8 $wt.\%$) and CaO (0.6–1.1 $wt.\%$) with A/CNK = 0.84–0.95. In addition, these volcanic rocks have low contents of Cr (<7.4 ppm) and Ni (<9.0 ppm)

(Figure 7A; Table S4). All samples are enriched in light rare earth elements (LREE) [(La/Yb) $_N$ = 8.57–14.12], show almost no fractionation between middle and heavy rare earth elements (HREE) [(Dy/Yb) $_N$ = 0.76–1.08], and display strongly negative Eu anomalies (Eu/Eu* = 0.23–0.37) (Figure 7B). On the primitive mantle-normalized trace element diagram, they are enriched in Pb, Th, Hf, Zr, and U and depleted in Ba, Nb, Sr, Ti, and Ta (Figure 7A). All Shiquanhe rhyolites on the total alkali-silica (TAS) diagram (Figure 8A) are further classified as part of the shoshonite series in the SiO_2 vs. K_2O diagram (Stern 2002; Figure 8B).
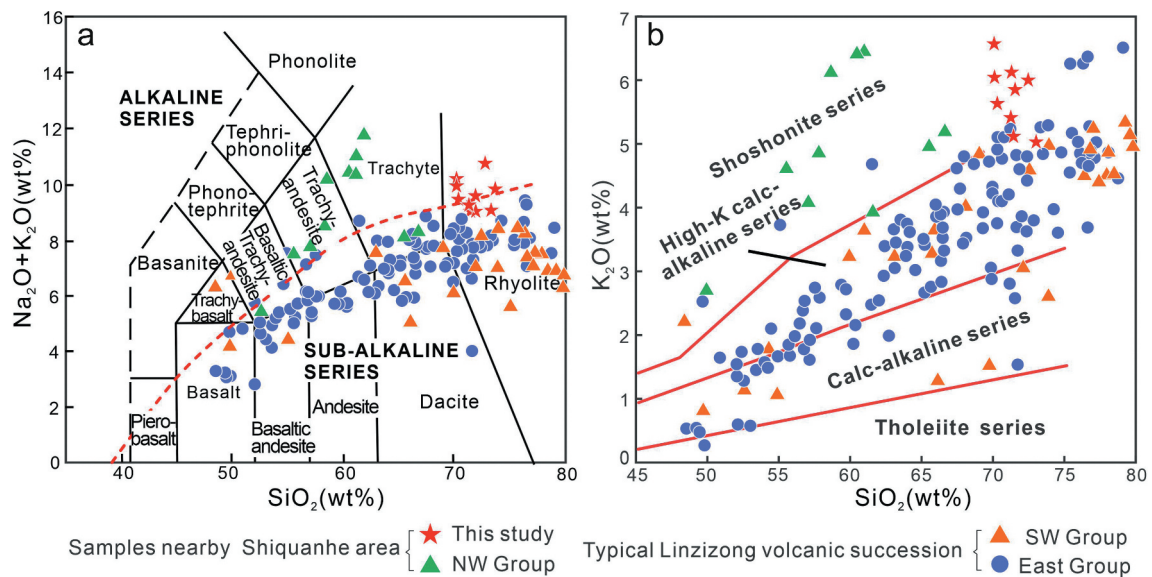

Figure 8. (A) Total alkali-silica diagram and (B) SiO_2 vs. K_2O diagram for samples from this study compared with data from the literature.
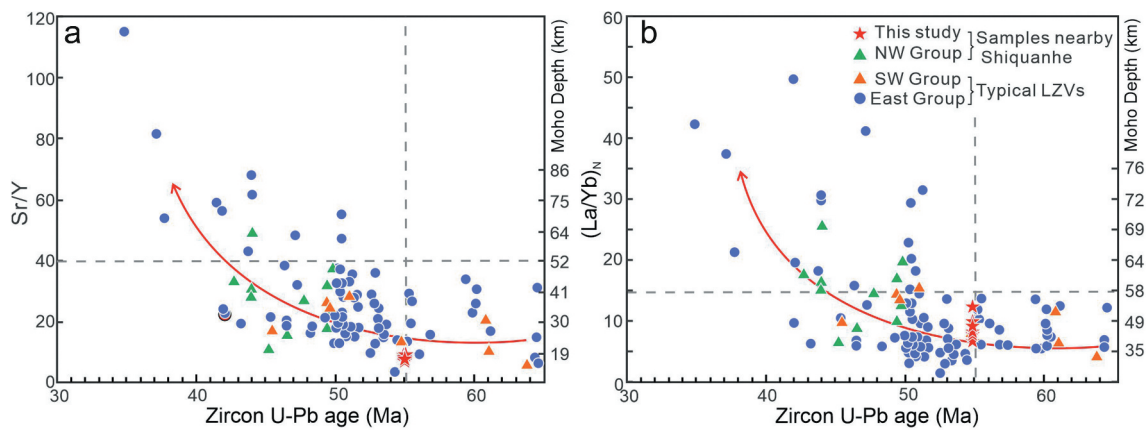
Figure 9. Plots of (A) Sr/Y and (B) La/Yb ratios vs. zircon U-Pb ages for samples along the Gangdese belt. The estimated melting depths are from .Lieu and Stern (2019)

5. Discussion

Below we use our new data to explore 5 aspects of Shiquanhe rhyolites: (1) the P-T environment in which these magmas formed; (2) their petrogenesis; (3) how Shiquanhe rhyolites differ from the LZVs; (4) what is the best geodynamic model to create Shiquanhe rhyolite melts; and (5) what implications do our new data and results have regarding the timing of the India–Eurasia collision and the far-field tectonic effect from this collision?

5.1. Melting models and P-T conditions

Euhedral zircons in the Shiquanhe rhyolites indicate that the magmas were saturated with zirconium (Figure 5A). The saturation behavior of zircon in crustal anatectic melts is a function of both temperature and composition (Watson and Harrison 1983; Boehnke et al. 2013). After the experimental calibration of zircon solubility in crustal melts, the function is given by: $lnD_{Zr}^{zircon/melt}$ = -(1.48 ± 0.09)-(1.16 ± 0.15)×(M-1)]+ (10,108 ± 32)/ (T-273.15), where $D_{Zr}^{zircon/melt}$ is the ratio of Zr concentration in zircons to that in the melt, M is the cation ratio (Na + K + 2Ca)/(Al·Si), and T is the Celsius temperature (Watson and Harrison 1983; Boehnke et al. 2013). The highest temperature calculated by the zircon saturation thermometer for our samples is 830℃ (Table S2). In addition, titanium concentrations in zircons can also reveal magmatic temperatures. Based on the Ti-in-zircon thermometer model (Schiller and Finger, 2019; Watson et al. 2006), zircon Ti contents in two Shiquanhe rhyolite samples (Ti = 20.5–44.3 ppm and 19.7–48.6 ppm) yield 908℃ and 917℃ as the highest crystallization temperatures. The results from the above thermometers agree; therefore, the temperature required to form these rhyolite magmas was ~900℃.

Partial melting or crystal fractionation to produce the Shiquanhe rhyolites can be inferred from residual or cumulate minerals (Menuge et al. 2002; Johnson and Plank 2000; Skora et al. 2015), and the nature of these phases can be revealed from specific trace elements (Menuge et al. 2002; Johnson and Plank 2000). Depletions in Sr and Eu are controlled by feldspar crystallization, and P 00depletion is controlled by apatite fractionation.

The Sr/Y ratio is especially useful for constraining the pressure of melting via the presence of minerals that fractionate Sr (plagioclase) vs. Y (amphibole and/or garnet) (Chiaradia 2015; Hu et al. 2020). Low Sr/Y ratios (average = 6.7) in the Shiquanhe rhyolites suggest low-pressure fractionation of amphibole and/or feldspar rather than high-pressure fractionation of garnet and/or amphibole (Figure 9A), which is consistent with the high HREE contents and low $(La/Yb)_N$ ratios (average = 10.14; Figure 9B). Therefore, considering the P-T conditions, the best melting model is a two-step process as follows: (1) shallow-middle feldspar-rich crust partially melted at >900℃ to form felsic magma, and (2) fractional crystallization of feldspar then formed the Shiquanhe rhyolite magma.

5.2. Petrogenesis

Shiquanhe rhyolites have high contents of SiO_2 and alkalis (K_2O and Na_2O), high FeO/MgO ratios, and low CaO, MgO, Al_2O_3, TiO_2, and P_2O_5 contents (Table S4). In the primitive mantle-normalized trace element diagram, the rhyolites are depleted in Ba, Nb, Sr, P, Eu, and Ti and enriched in Rb, Y, and high field strength elements (Figure 7A). In the chondrite-normalized REE pattern diagram, samples show distinct negative Eu anomalies and enriched LREEs

(Figures 7B). These above geochemical signatures are similar to some other subduction-related magmatic products. However, according to the high Fe/Mg and Ga/Al ratios and high temperatures, Shiquanhe rhyolites are A-type rhyolites (Whalen *et al*. 1987; Eby 1992; Zhang *et al*. 2007). It is also important to note that Shiquanhe rhyolites have high SiO_2 contents, which are similar to those of highly fractionated rhyolites. Highly fractionated rhyolites generally contain >70 wt.% SiO_2 and are typically enriched in REEs and lithophile elements relative to crustal abundances (e.g. Rudnick and Gao, 2003). Previous studies have demonstrated that highly fractionated granites may have compositions overlapping those of typical A-type granites (Whalen *et al*. 1987; Chappell and White 1992; King *et al*. 1997). The magmatic system would gradually decrease its temperature during differentiation; therefore, the Zr concentration of the magma would be decreased in the highly fractionated magma since it is closely related to the temperature (Boehnke *et al*. 2013;

Watson and Harrison 1983; Watson *et al*. 2006; Figure 10C). In contrast, A-type rhyolites are characterized by their high magma temperatures and have another evolved trend, as shown in Figure 10C. On the other hand, zircon, as an important accessory mineral in highly fractionated granitic rocks, crystallizes earlier in weakly fractionated granite than in highly fractionated granite (Breiter *et al*. 2014). Under this situation, both whole-rock and zircons of highly fractionated granitic rocks show much lower Zr/Hf ratios than commonly observed (Bau 1996; Deering *et al*. 2016). Therefore, the high Zr/Hf ratios of the Shiquanhe rhyolites (Zr/Hf = 28.1–33.3) are not consistent with those of highly evolved rhyolites (Zr/Hf ratios<25; Breiter *et al*. 2014). Through the above comparison and exclusion, the Shiquanhe rhyolites are A-type felsic magmas (Whalen *et al*. 1987; Frost and Frost 2013), as supported by Nb *vs*. Zr, FeO*/MgO *vs*. Na_2O+K_2O and Zr *vs*. Ga/Al diagrams (Figure 10A, B and C). The term 'A-type' is synonymous with the term 'ferroan'; the latter has been
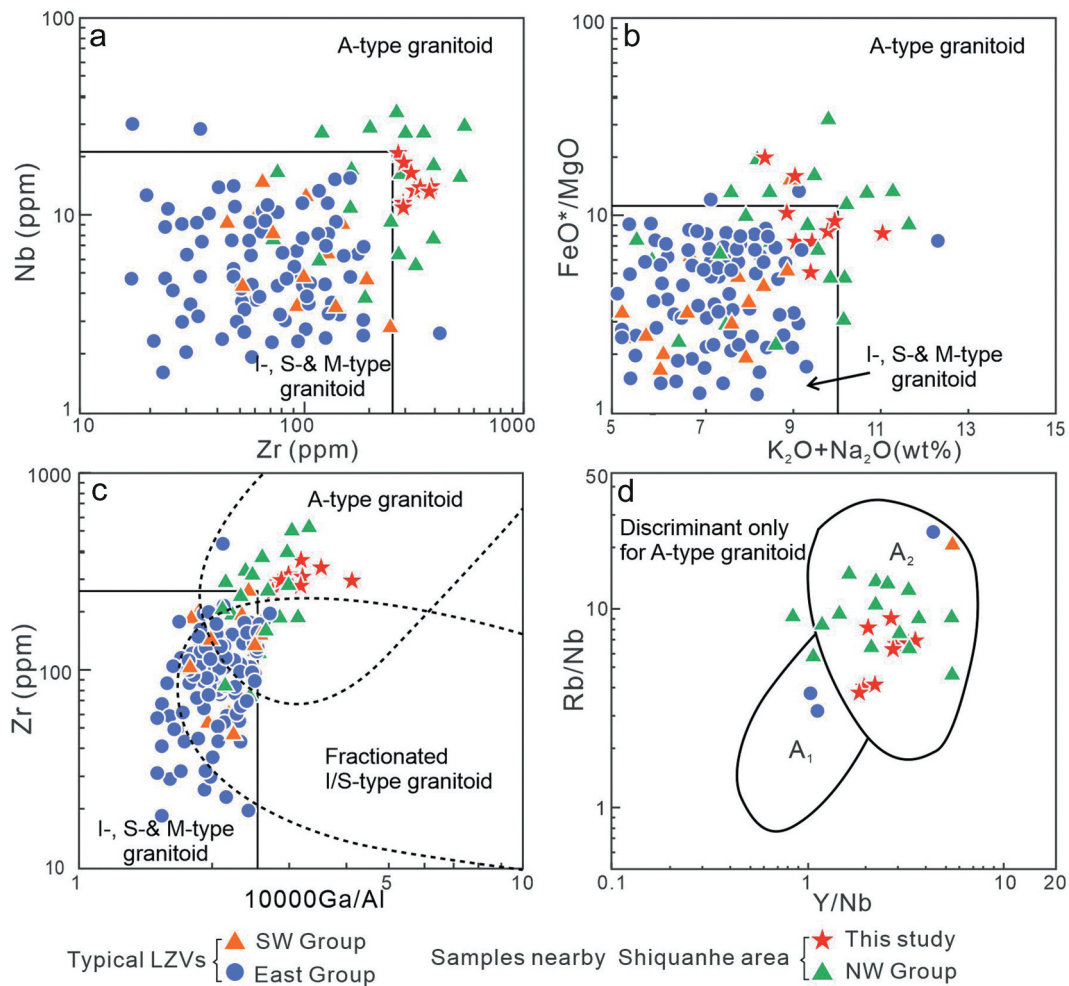

Figure 10. A-type granite discrimination diagram. A, B and C are after Whalen *et al*. (1987); D is after Eby (1992). A_1 - anorogenic A-type granitic rocks, A_2 - post-collisional A-type granitic rocks, the dotted lines distinguished the A-type granitic rocks and highly fractionated granitic rocks are from Wu et al. (2017).

suggested to replace the use of 'A-type' (Frost *et al*. 2001; Frost and Frost 2011). Based on the geochemical classification from Frost and Frost (2011), Shiquanhe A-type rhyolites are peraluminous ferroan granitoids formed from partial melting of quartz-feldspathic crust. In this study, we still use the 'A-type' term, which gives more detailed insight into petrogenesis as follows.

A-type granites/rhyolites were first defined by Loiselle and Wones (1979) and have since received extensive attention and discussion (Collins *et al*. 1982; Whalen *et al*. 1987; Eby 1992; Bonin 2007; Zhang *et al*. 2007). A-type melts occurred worldwide throughout geological time in a variety of tectonic settings and generally but not necessarily indicate an anorogenic or rifting environment (Whalen *et al*. 1987; Bonin 2007). However, A-type melts are generally considered to have a source of dehydrated, reasonably salic crust, and a source of high heat sufficient to partially melt this crust (Whalen *et al*. 1987; Bonin 2007). The heat supply could be from the upwelling asthenosphere after lithosphere thinning (delamination or rifting) or hot materials coming from below as mantle plumes (Black and Liégeois, 1993; Bonin 2007). The above two heat sources correspond to two magmatic processes and form two subtypes of A-type rocks (Eby 1992). These two subtypes can be effectively subdivided on the Rb/Nb vs. Y/Nb diagram (Figure 10D). A_1 granitic rocks formed by mantle melting with continental contamination in an extensional tectonic setting, similar to that of intraplate or rift-zone magmas (Eby 1992). A_2-type magmas are thought to originate from partial melting of continental crust or underplated crust following continent-continent collision (Eby 1992; Figure 10D). The higher Y/Nb and Yb/Ta ratios in the A_2 group indicate a source from partial melting of pre-existing crust. Shiquanhe rhyolites are typical of the A_2 group (Figure 10D).

Zircon Lu–Hf isotope compositions can help reveal crustal evolution (Kinny and Maas 2003). Granitic rocks in the east and southwest Gangdese belt are characterized by highly positive zircon $\varepsilon_{Hf}(t)$ values, indicating that the magma was derived from juvenile crust (Figure 6). However, an increasing number of studies show that Eocene granitic rocks in northwest Gangdese have negative zircon εHf(t) values, indicating that ancient crust was involved (e.g. Wang *et al*. 2015b; Huang *et al*. 2019). Shiquanhe rhyolites exhibit slightly positive zircon $\varepsilon_{Hf}(t)$ values (+2.5 to +4.4) and 750 to 850 Ma model ages, consistent with partial melting of ancient lithosphere. In addition, the zircon $\varepsilon_{Hf}(t)$ values from the Gangdese belt decrease with age, reaching a minimum during the Eocene (~55 Ma) (Figure 6). This trend requires increasing involvement of old crust with time (Ji *et al*. 2009). The North Lhasa Terrane and South Qiangtang Terrane near the Shiquanhe area could be the source of the old crust. However, igneous rocks of the North Lhasa Subterrane have a peak age at 130 ± 5 Ma with low T_{DM}^C (<0.8 Ga) and high zircon εHf(t) values (> +12), indicating a juvenile source (Zhu *et al*. 2011; Hou *et al*. 2015). In addition, the oldest intrusive rocks found in the North Lhasa Subterrane are Early Jurassic granodiorites (185–181 Ma) (Li *et al*. 2021aa). Therefore, the Shiquanhe rhyolites should have been sourced from partial melting of South Qiangtang crust, which can provide more ancient sources (Hu *et al*. 2015; Dan *et al*. 2020).

The heat source for partial melting is also key for understanding Shiquanhe rhyolite petrogenesis. High-silica A-type rhyolite petrogenesis requires sustained high heat flow (Zhang *et al*. 2007; Frost and Frost 2011). Considering the HT-LP melting conditions, five mechanisms could have provided this heat: (1) a mantle plume (Zheng *et al*. 2019); (2) lithospheric extension during continental rifting or back-arc magmatism; (3) crustal extension along a major detachment fault (Viruete 1999; Dokuz 2011); (4) pervasive flow of melt (Miyazaki 2004); and (5) mantle asthenosphere upwelling after oceanic slab break-off or lithospheric delamination (Chapman *et al*. 2018). Mantle plumes and LIPs can generate voluminous high-temperature magmas with A-type geochemical characteristics. However, the lack of synchronous massive oceanic island basalts (OIBs) and continental flood basalts (CFBs) in the region does not support this model (Wignall 2001; Niu *et al*. 2011). Lithospheric extension is inconsistent with a compressional tectonic setting along the BNSZ during the early Eocene (Kapp and DeCelles 2019). Sufficient basaltic melt is thought to be capable of raising crustal temperature to 800°C at 15 km depth (Miyazaki 2004), which almost meets the Shiquanhe rhyolite melting conditions. However, the lack of injected mafic magmas is evidence against such a process (Miyazaki 2004; Dokuz 2011). Because Shiquanhe rhyolites are located on the SW Qiangtang margin, we connect the heat source with mantle upwelling after oceanic slab break-off or lower continental crust delamination. Recent studies in the eastern Gangdese belt suggest that the Neotethyan oceanic slab break-off started at ~57 Ma with slab tearing (Huang *et al*. 2017, 2020; Tian *et al*. 2021). However, the magmatic 'flare-up' and crustal growth caused by the Neotethyan oceanic slab break-off started at ~48–40 Ma (Xu *et al*. 2008; Lee *et al*. 2009; Ma *et al*. 2016), significantly younger than the Shiquanhe rhyolites. After considering all possible heat sources, we think that the upwelling asthenosphere following lithospheric delamination was the most likely heat source for generating Shiquanhe rhyolites.

Notably, Shiquanhe rhyolite La/Yb and Sr/Y ratios increase with time (Figure 9). These ratios reflect the

pressure at which melting and fractionation occurred and can proxy for crustal thickness (Lieu and Stern 2019; Hu *et al*. 2020). It is difficult to pinpoint on Figure 9 when Tibetan crust began to thicken, but this seems to be ~50 Ma. Therefore, partial melting of ancient SW Qiangtang crust accompanied crustal thickening after the Early Eocene (~55 Ma) and may have been responsible for Shiquanhe rhyolite petrogenesis (Figure 9).

5.3. Comparison of Shiquanhe rhyolites with typical Linzizong volcanic rocks (LZVs)

Abundant Eocene magmatic rocks are found along the Gangdese magmatic belt (Figures 1 and 2; Table S1). We divide these rocks into the East, Northwest, and Southwest Groups to discuss their characteristics and evolution. The Northwest Group includes Eocene volcanic rocks around the Shiquanhe area. Both the East and Southwest Groups represent typical LZVs. Obviously, the Northwest Group does not share the same petrogenetic model with the LZVs (the East and Southwest Groups). This is reflected in the following observations: (1) Southward migration of LZVs (the East Group and the Southwest Group) caused by Neotethyan oceanic slab rollback is inconsistent with the far northern position of the Northwest Group (Lee *et al*. 2012; Wang *et al*. 2015b; Ji *et al*. 2009; Figures 1B and 2B). (2) The part of the LZVs caused by Neotethyan Oceanic slab break-off cannot match the sharp decrease in zircon Hf isotopes of the Northwest Group at ~55 Ma (Wang *et al*. 2015b; Ji *et al*. 2009, 2012; Figure 6). In other words, the Northwest Group has lower zircon $\varepsilon_{Hf}(t)$ values than the other two groups. (3) The Northwest Group is richer in trace elements with crustal affinity (such as Pb, Zr, Hf, and Th) and has distinctly negative Eu anomalies (Figure 7). (4) The Northwest Group is richer in large ion lithophile elements (LILEs) and is assigned to the shoshonite series, while most LZVs from the other two groups are calc-alkaline (Figure 8). (5) Northwest Group rhyolites exhibit distinct A_2-type characteristics, suggesting a high magmatic temperature and a non-subduction setting; however, typical LZVs display an affinity with subduction (Figure 10). In summary, it is difficult to explain these three groups of rocks with a single model. Roll-back and break-off of the Neotethyan Oceanic slab might explain the formation of East and Southwest Group (typical LZVs), but the Northwest Group was produced by lithospheric delamination with sources from melting crust and upwelling asthenosphere.

5.4. Geodynamic model

The Gangdese magmatic belt records magmatic activity related to the northward subduction of the Neotethyan Ocean and the India–Eurasia collision. These igneous rocks with ages from 65 Ma to 45 Ma are considered products of Neotethyan Oceanic slab roll-back and break-off during the late stage of northward subduction (Haschke *et al*. 2002; Lee *et al*. 2009; Zhang *et al*. 2012; Wang *et al*. 2015a). This time interval also marks a key transition from ocean-continent subduction to continued continental subduction (Replumaz *et al*. 2016). However, A-type (ferroan) rhyolites around the Shiquanhe area cannot fit the above model, and there should be an independent tectonic-magmatic process to explain them. Based on field geological surveys, whole-rock geochemistry and zircon geochronology, we suggest local lithospheric delamination beneath the SW Qiangtang margin. The evolution of this process and interpretations compatible with previous models are described as follows (Figure 11):

Step 1. Qiangtang–Lhasa collision and South Qiangtang Terrane (SQT) delamination (Cretaceous)

Lower Cretaceous strata in the Baingoin basin record the initial collision between the Lhasa Terrane and Qiangtang Terrane (Lai *et al*. 2019). The Nima area underwent major deformation and was uplifted above sea level between ca. 125 Ma and ca. 118 Ma, which also suggests Early Cretaceous crustal thickening caused by the Lhasa–Qiangtang collision (Kapp *et al*. 2007). In addition, many Late Cretaceous (85–95 Ma) Mg-rich and adakitic rocks are recognized along the BNSZ, which are interpreted as consequences of lithospheric foundering along the Lhasa–Qiangtang collision zone (Lustrino 2005; Wang *et al*. 2014a; Yi *et al*. 2018; Liu *et al*. 2019). These lines of evidence demonstrate that the Qiangtang Terrane and Lhasa Terrane collided during the Cretaceous, and that crustal thickening has occurred along the BNSZ in the western and central Tibet since the Late Cretaceous (Figure 11). However, recent research proposed a diachronous collision of the Lhasa Terrane with the Southern Qiangtang Terrane during 145 Ma to 120 Ma, which led to eastward propagating slab tearing and asthenospheric upwelling over time (Gao and Dilek 2022).

Step 2. Neotethyan Oceanic slab roll-back and LZV southward migration (Late Cretaceous–Paleocene)

Near the end of the Late Cretaceous (~69 Ma), the India–Eurasia convergence rate increased from ~12 to ~17 cm/year and then decreased to ~10 cm/year in the Paleocene (~58 Ma) (Lee and Lawver 1995; Wang *et al*. 2015a). Next the plate motion of India slowed dramatically in the Eocene (between 50 Ma and 35 Ma), with a rate of 4 cm/year (Copley *et al*. 2010). These changes are coincident with the slab roll-back related to the
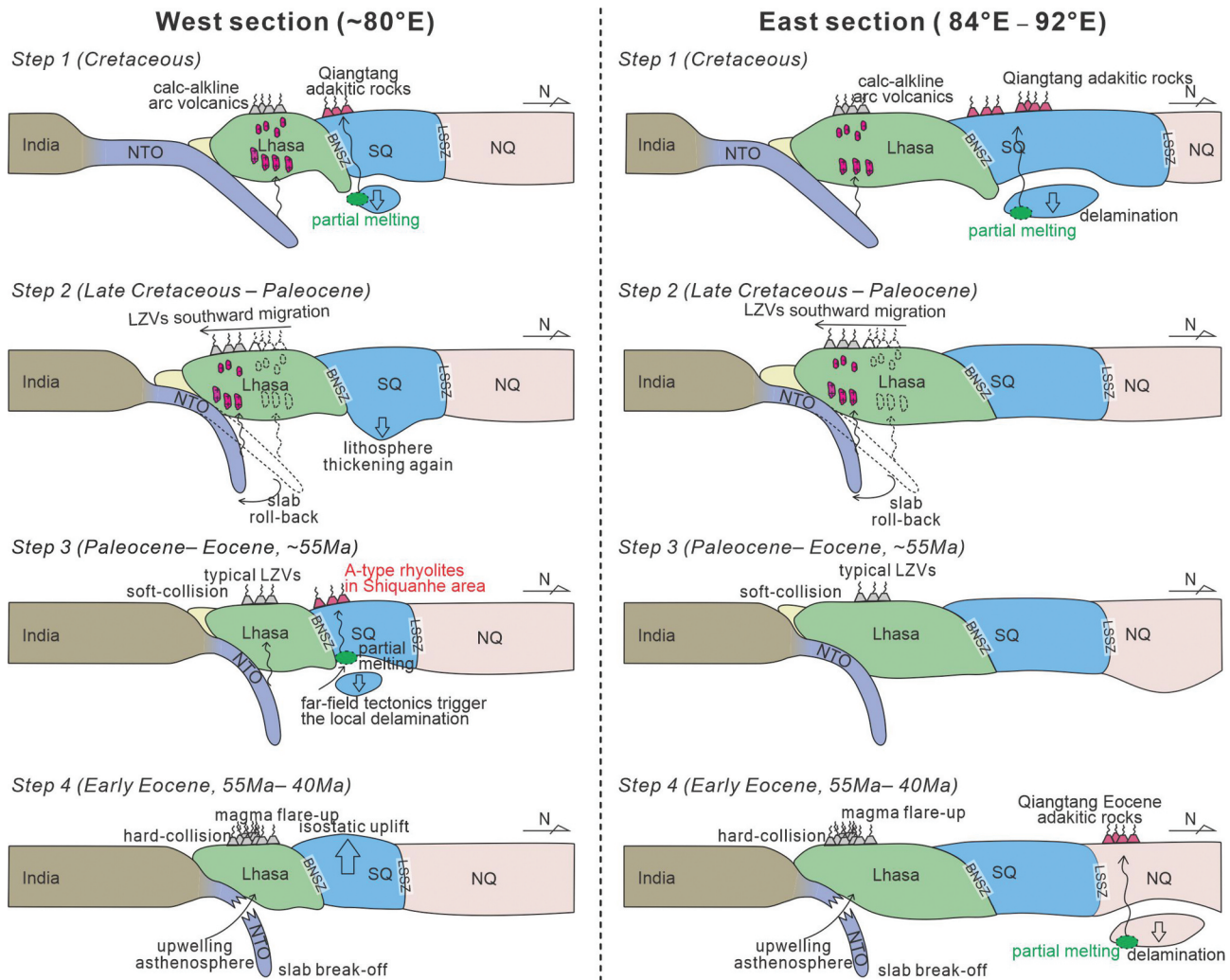
Figure 11. Geodynamic model of the tectonic and magmatic evolution related to the India–Eurasia collision is shown for the western and eastern sections.

northward subduction of the Neotethyan Ocean and produced a southward migration of magmatism. Neotethyan Oceanic slab roll-back is widely accepted as a 'last gasp' before India–Eurasia collision (Dilek and Flower, 2003). From the Qiangtang–Lhasa collision until the Eocene, the Tibetan Plateau was continually squeezed from north to south. There is almost no magmatic record around the Shiquanhe area, after the latest delamination caused by Lhasa–Qiangtang collision. Therefore, the lithosphere in the western BNSZ around the Shiquanhe area continued to thicken over the next ~30 Myr (Figure 11).

Step 3. India–Eurasia collision and the far-field tectonic effect (Paleocene–Eocene, ~55 Ma)

Although when the India-Eurasia collision began and how it evolved remain controversial, most studies put the timing closer to 55 Ma, or slightly earlier (Ji *et al*. 2012; Hu *et al*. 2016; Motuza and Šliaupa 2017; Zhu *et al*.

2019). At the same time, the Shiquanhe delamination occurred around the Early Eocene (~55 Ma). Such synchronicity has been interpreted to result from stress transfer from the YTSZ to the foreland during India–Eurasia continental collision. Long-term subduction, arc magmatism, and crustal thickening along the southern margin of Eurasia weakened Lhasa Terrane lithosphere (Yin and Harrison 2000). Studies confirm that hot and weak continental lithosphere can transmit stress across thousands of kilometers (Kearey *et al*. 2009; Najman *et al*. 2017). Therefore, Shiquanhe delamination was most likely initiated by a far-field tectonic effect caused by India–Eurasia collision with a pre-thickened South Qiangtang lithosphere. This kind of far-field effect could allow the strong compressive stress to penetrate northward into the plateau's interior and trigger delamination. The far-field tectonic effect has been widely verified in Egypt Syrian arc area and Arabia–Eurasia collision area by thermochronological data and tectonic

observation (Albino *et al.*, 2014; Bosworth *et al.* 1999; Cavazza *et al.* 2017; Gusmeo *et al.* 2021), while this is the first time that the far-field tectonic effect has been applied to the India–Eurasia collision zone.

This above model reveals a small-scale (around the Shiquanhe area) lithospheric delamination in the SW Qiangtang terrane (Figure 11). We propose two possible factors to explain the limited distribution of the A-type rhyolites: (1) the Shiquanhe area, the western Tibetan Plateau, experienced stronger compression and more significant shortening, which can provide sufficient far-field extrusion stress for the delamination (Kapp *et al.* 2003; Kapp and DeCelles 2019); (2) It is a widely held notion that since collision between Lhasa Terrane and Qiangtang Terrane, the tectonic stress regime along the BNSZ changed from shortening (thrusting and reverse faulting) to strike-slip faulting with vertical thickening. Such a tectonic change is supported by palaeomagnetic data (Torsvik *et al.* 2012; Song *et al.* 2017). Based on a progressive eastward younging of Albian–Cenomanian granitoids, a diachronous Lhasa–Qiangtang collision with eastward propagated slab tearing has been proposed (Gao and Dilek 2022 and references therein). Therefore, western South Qiangtang experienced longer compression than the eastern part, resulting in more pronounced lithospheric thickening. Lastly, our results for A-type rhyolites around the Shiquanhe area suggest that India–Eurasia collision in central-western Tibet (~80°E) began before ~55 Ma.

Step 4. Neotethyan Oceanic slab break-off and formation of Eocene adakitic rocks (Early Eocene, 55–40 Ma)

During the Early Eocene (ca. 51–46 Ma), an episode of intense magmatism flared up along the Gangdese belt, driven by Neotethyan oceanic slab break-off (e.g. Chung *et al.* 2005; Ji *et al.* 2009). Tensile stresses caused by the different buoyancies of the Lhasa continental lithosphere and previously subducted Neotethyan oceanic lithosphere led to a slab tear that formed a slab window after collision began (van Hunen and Allen 2011). The asthenosphere welled up through the slab window to produce various magmas from tholeiitic basalts to Eocene adakitic rocks in the Qiangtang Terrane (e.g. Chung *et al.* 2005; Mo *et al.* 2007; Lee *et al.* 2009; Zeng *et al.* 2020). The narrow time span and the linear distribution of the Eocene LZVs along the Gangdese belt seem to agree with the focused heat source, which can be better explained by mantle upwelling in association with slab break-off (Davies and von Blanckenburg 1995; Dokuz 2011; Altunkaynak *et al.* 2012). We prefer that the India-Asia collision led to the negative buoyancy of subducted continental lithosphere in the collision zone. This process can then lead into lithospheric necking and breakoff, generating an asthenospheric window and influx of heat and hot mantle material upwards, which is similar to the slab break-off case studies in Anatolia, Azerbaijan and NW Iran (Dilek and Altunkaynak 2007, 2009; Dilek *et al.* 2010; Altunkaynak *et al.* 2012).

6. Conclusions

Eocene rhyolites around the Shiquanhe area (southwestern Qiangtang margin) are A-type (ferroan) granitoids with post-collisional affinities. There are two series of igneous rocks with different petrogeneses that developed at ~55 Ma and ~48 Ma in the western Gangdese belt, the Shiquanhe rhyolites and the Linzizong volcanics. Crustal delamination produced the former series, and the latter series was the product of Neotethyan Oceanic slab break-off. We interpret the Eocene delamination beneath the Shiquanhe area as the result of stress transfer from the India–Eurasia collision zone towards the Eurasia foreland, which is a far-field tectonic effect. Based on this model, the time of the India–Eurasia collision in the western Tibetan Plateau is constrained to ~55 Ma ago.

Highlights

- A-type rhyolites with an age of ~55 Ma in southwest Tibet have a post-collision affinity.
- Delamination could relate to a far-field tectonic induced by continental collision.
- In the Shiquanhe area, southwest Tibet, the India-Eurasia collided before ~55 Ma.
- The lithosphere delamination is anisotropic with various locations and intensities.

Disclosure statement

No potential conflict of interest was reported by the author(s).

Funding

ORCID

Chenwei Li 🆔 http://orcid.org/0000-0002-4243-1170

References

Albino, I., Cavazza, W., Zattin, M., Okay, A.I., Adamia, S., and Sadradze, N., 2014. Far-field tectonic effects of the Arabia–Eurasia collision and the inception of the North Anatolian fault system. Geol. Mag. 151, 372–379.

Altunkaynak, Ş., Sunal, G., Aldanmaz, E., Genç, C.Ş., Dilek, Y., Furnes, H., Foland, K.A., Yang, J., and Yıldız, M., 2012. Eocene granitic magmatism in NW Anatolia (Turkey) revisited: New implications from comparative zircon SHRIMP U–Pb and 40Ar–39Ar geochronology and isotope geochemistry on magma genesis and emplacement. Lithos 155, 289–309.

Bau, M., 1996. Controls on the fractionation of isovalent trace elements in magmatic and aqueous systems: Evidence from Y/Ho, Zr/Hf, and lanthanide tetrad effect. Contrib Mineral Petr 123, 323–333.

Bi, W., Han, Z., Li, Y., Li, C., Wang, C., Zhang, J., Han, J., He, H., Qian, X., Xu, T., and Ma, Z., 2020. Deformation and cooling history of the Central Qiangtang terrane, Tibetan Plateau and its tectonic implications. Int Geol Rev 63, 1821–1837.

Black, R., and Liegeois, J., 1993. Cratons, mobile belts, alkaline rocks and continental lithospheric mantle: The Pan-African testimony. J Geol Soc London 150, 89–98.

Boehnke, P., Watson, E.B., Trail, D., Harrison, T.M., and Schmitt, A.K., 2013. Zircon saturation re-revisited. Chem Geol 351, 324–334.

Bonin, B., 2007. A-type granites and related rocks: Evolution of a concept, problems and prospects. Lithos 97, 1–29.

Bosworth, W., Guiraud, R., and Kessler, L.G., 1999. Late Cretaceous (ca. 84 Ma) compressive deformation of the stable platform of northeast Africa (Egypt): Far-field stress effects of the "Santonian event" and origin of the Syrian arc deformation belt. Geology 27, 633–636.

Breiter, K., Lamarão, C.N., Borges, R.M.K., and Dall'Agnol, R., 2014. Chemical characteristics of zircon from A-type granites and comparison to zircon of S-type granites. Lithos 192, 208–225.

Cavazza, W., Albino, I., Zattin, M., Galoyan, G., Imamverdiyev, N., and Melkonyan, R., 2017. Thermochronometric evidence for Miocene tectonic reactivation of the Sevan–Akera suture zone (Lesser Caucasus): A far-field tectonic effect of the Arabia–Eurasia collision? Geological Society, London, Special Publications 428, 187–198.

Chapman, J.B., Scoggin, S.H., Kapp, P., Carrapa, B., Ducea, M.N., Worthington, J., Oimahmadov, I., and Gadoev, M., 2018. Mesozoic to Cenozoic magmatic history of the Pamir. Earth Planet Sci Lett 482, 181–192.

Chappell, B.W., and White, A., 1992. I-and S-type granites in the Lachlan Fold Belt. Earth Env Sci T R so 83, 1–26.

Chen, W.Y., Hu, X.C., Zhong, Y., Fu, Y.B., Li, F., and Wang, Y.G., 2018. Comment on "Sedimentary and tectonic evolution of the southern Qiangtang basin: Implications for the Lhasa-Qiangtang collision timing" by A. Ma Et Al.: Journal of Geophysical Research: Solid Earth, v. 123, no. 9, p. 7338–7342.

Chen, C., Yang, X., Wang, X., Zeng, D., Feng, M., Xie, L., and Li, X., 2020. Pore-fillings of dolomite reservoirs in Sinian Dengying Formation in Sichuan basin. Petroleum 6, 14–22.

Chiaradia, M., 2015. Crustal thickness control on Sr/Y signatures of recent arc magmas: An Earth scale perspective. Sci Rep–Uk 5, 81–15.

Chu, M., Chung, S., Song, B., Liu, D., O'Reilly, S.Y., Pearson, N.J., Ji, J. and Wen, D., 2006. Zircon U-Pb and Hf isotope constraints on the Mesozoic tectonics and crustal evolution of southern Tibet: Geology, v. 34, no. 9, p. 745–748.

Chung, S., Chu, M., Zhang, Y., Xie, Y., Lo, C., Lee, T., Lan, C., Li, X., Zhang, Q., and Wang, Y., 2005. Tibetan tectonic evolution inferred from spatial and temporal variations in post-collisional magmatism. Earth-Sci Rev 68, 173–196.

Collins, W.J., Beams, S.D., White, A.J.R., and Chappell, B.W., 1982. Nature and origin of A-type granites with particular reference to southeastern Australia Contributions to mineralogy and petrology, v. 80, no. 2, p. 189–200.

Cong, Y., Xiao, K., Zhai, Q. and Dong, Q., 2012. LA- ICP- MS Dating and Hf Isotopic Analysis of the Zircon from the Puluogang Granite in Namulin County, Tibet, and Its Geological Significance: Journal of Jilin University(Earth Science Edition), v. 42, no. 6, p. 1783–1795.

Copley, A., Avouac, J.P., and Royer, J.Y., 2010. India-Asia collision and the Cenozoic slowdown of the Indian plate: Implications for the forces driving plate motions. Journal of Geophysical Research: Solid Earth, 115(B3 1–14).

Dan, W., Wang, Q., Zhang, X., and Tang, G., 2020. Early Paleozoic S-type granites as the basement of Southern Qiangtang Terrane, Tibet. Lithos 356, 105–395.

Davies, J.H., and von Blanckenburg, F., 1995. Slab break-off: A model of lithosphere detachment and its test in the magmatism and deformation of collisional orogens. Earth Planet Sc Lett 129, 85–102.

Deering, C.D., Keller, B., Schoene, B., Bachmann, O., Beane, R., and Ovtcharova, M., 2016. Zircon record of the plutonic-volcanic connection and protracted rhyolite melt evolution. Geology 44, 267–270.

Dilek, F., 2003. Arc-trench roll-back and forearc accretion: 2. A model template for ophiolites in Albania, Cyprus, and Oman. Geological Society London 218, Special Publication, 43–68.

Dilek, Y., and Altunkaynak, Ş., 2007. Cenozoic crustal evolution and mantle dynamics of post-collisional magmatism in western Anatolia. Int. Geol. Rev. 49, 431–453.

Dilek, Y., and Altunkaynak, Ş., 2009. Geochemical and temporal evolution of Cenozoic magmatism in western Turkey: Mantle response to collision, slab break-off, and lithospheric tearing in an orogenic belt. Geological Society, London, Special Publications 311, 213–233.

Dilek, Y., Imamverdiyev, N., and Altunkaynak, Ş., 2010. Geochemistry and tectonics of Cenozoic volcanism in the Lesser Caucasus (Azerbaijan) and the peri-Arabian region: Collision-induced mantle dynamics and its magmatic fingerprint. Int. Geol. Rev. 52, 536–578.

Ding, L., Xu, Q., Yue, Y., Wang, H., Cai, F., and Li, S., 2014. The Andean-type Gangdese Mountains: Paleoelevation record from the Paleocene–Eocene Linzhou Basin. Earth Planet Sci Lett 392, 250–264.

Dokuz, A., 2011. A slab detachment and delamination model for the generation of Carboniferous high-potassium I-type magmatism in the Eastern Pontides, NE Turkey: The Köse composite pluton. Gondwana Res 19, 926–944.

Dong, X., 2008. The geochronology and geochemistry of the Mesozoic and Cenozoic granitoids from southwestern Gangdese belt, Tibet: Master Degree Thesis. Beijing: China University of Geosciences, v. 1, p. 1–94.

Dong, X., Zhang, Z., and Santosh, M., 2010. Zircon U-Pb chronology of the Nyingtri group, southern Lhasa terrane, Tibetan Plateau: Implications for Grenvillian and Pan-African provenance and Mesozoic-Cenozoic metamorphism. The Journal of Geology 118, 677–690.

Draut, A.E., and Clift, P.D., 2013. Differential preservation in the geologic record of intraoceanic arc sedimentary and tectonic processes. Earth-Sci Rev 116, 57–84.

Eby, G.N., 1992. Chemical subdivision of the A-type granitoids: Petrogenetic and tectonic implications. Geology 20, 641–644.

Festa, A., Pini, G.A., Dilek, Y., and Codegone, G., 2010. Mélanges and mélange-forming processes: A historical overview and new concepts: International Geology Review, v. 52, no. 10–12, p. 1040–1105.

Festa, A., Pini, G.A., Ogata, K., and Dilek, Y., 2019. Diagnostic features and field-criteria in recognition of tectonic, sedimentary and diapiric mélanges in orogenic belts and exhumed subduction-accretion complexes: Gondwana Research, v. 74, p. 7–30.

Frost, B.R., Barnes, C.G., Collins, W.J., Arculus, R.J., Ellis, D.J., and Frost, C.D., 2001. A geochemical classification for granitic rocks. J Petrol 42, 2033–2048.

Frost, C.D., and Frost, B.R., 2011. On ferroan (A-type) granitoids: Their compositional variability and modes of origin. J Petrol 52, 39–53.

Frost, B.R., and Frost, C.D., 2013. Essentials of igneous and metamorphic petrology, Cambridge: Cambridge University Press.

Gao, X., and Dilek, Y., 2022. Albian– Cenomanian granitoid magmatism in Eastern and Central Tibet as a result of diachronous, continental collision induced slab tear propagation: GSA Bulletin, 1–20.

Grimes, C.B., John, B.E., Kelemen, P.B., Mazdab, F.K., Wooden, J.L., Cheadle, M.J., Hanghøj, K., and Schwartz, J.J., 2007. Trace element chemistry of zircons from oceanic crust: A method for distinguishing detrital zircon provenance. Geology 35, 643–646.

Guan, Q., Zhu, D., Zhao, Z., Dong, G., Zhang, L., Li, X., Liu, M., Mo, X., Liu, Y. and Yuan, H., 2012. Crustal thickening prior to 38 Ma in southern Tibet: evidence from lower crust-derived adakitic magmatism in the Gangdese Batholith: Gondwana Research, v. 21, no. 1, p. 88–99.

Guo, Z., Wilson, M., and Liu, J., 2007. Post-collisional adakites in south Tibet: Products of partial melting of subduction-modified lower crust. Lithos 96, 205–224.

Gusmeo, T., Cavazza, W., Alania, V.M., Enukidze, O.V., Zattin, M., and Corrado, S., 2021. Structural inversion of back-arc basins–The Neogene Adjara–Trialeti fold-and-thrust belt (SW Georgia) as a far-field effect of the Arabia-Eurasia collision. Tectonophysics 803, 228–702.

Gutscher, M.A., Maury, R., Eissen, J.P., and Bourdon, E., 2000. Can slab melting be caused by flat subduction? Geology 28, 535–538.

Haschke, M., Siebel, W., Günther, A., and Scheuber, E., 2002. Repeated crustal thickening and recycling during the Andean orogeny in North Chile (21°–26°S). Journal of Geophysical Research Atmospheres 107, 1–18.

Heuberger, S., Schaltegger, U., Burg, J., Villa, I.M., Frank, M., Dawood, H., Hussain, S. and Zanchi, A., 2007. Age and isotopic constraints on magmatism along the Karakoram-Kohistan Suture Zone, NW Pakistan: Evidence for subduction and continued convergence after India-Asia collision: Swiss Journal of Geosciences, v. 100, no. 1, p. 85–107. 10.1007/s00015-007-1203-7

Hoskin, P.W.O., and Schaltegger, U., 2003. The Composition of Zircon and Igneous and Metamorphic Petrogenesis. Rev. miner.geochem 53, 27–62.

Hou, Z., Duan, L., Lu, Y., Zheng, Y., Zhu, D., Yang, Z., Yang, Z., Wang, B., Pei, Y., and Zhao, Z., 2015. Lithospheric architecture of the Lhasa terrane and its control on ore deposits in the Himalayan–Tibetan orogen. Econ Geol 110, 1541–1575.

Hu, X., Garzanti, E., Wang, J., Huang, W., An, W., and Webb, A., 2016. The timing of India-Asia collision onset – Facts, theories, controversies. Earth-Sci Rev 160, 264–299.

Hu, Z., Liu, Y., Gao, S., Liu, W., Zhang, W., Tong, X., Lin, L., Zong, K., Li, M., and Chen, H., 2012. Improved in situ Hf isotope ratio analysis of zircon using newly designed X skimmer cone and jet sample cone in combination with the addition of nitrogen by laser ablation multiple collector ICP–MS. J Anal Atom Spectrom 27, 1391–1399.

Hu, H., and Stern, R.J., 2020. Early Cretaceous Subduction Initiation in Southern Tibet Caused the Northward Flight of India. Geoscience Frontiers 11, 1123–1131.

Hu, F., Wu, F., Chapman, J.B., Ducea, M.N., Ji, W., and Liu, S., 2020. Quantitatively Tracking the Elevation of the Tibetan Plateau Since the Cretaceous: Insights From Whole-Rock Sr/Y and La/Yb Ratios. Geophys Res Lett 47, 1–10.

Hu, P.Y., Zhai, Q.G., Jahn, B.M., Wang, J., Li, C., Lee, H.Y., and Tang, S.H., 2015. Early Ordovician granites from the South Qiangtang terrane, northern Tibet: Implications for the early Paleozoic tectonic evolution along the Gondwanan proto-Tethyanmargin. Lithos 220, 318–338.

Huang, F., Xu, J., Wang, B., Zeng, Y., Liu, X., Liu, H., and Yu, H., 2020. Destiny of Neo-Tethyan Lithosphere during India–Asia Collision. Earth Science 45, 2785–2804.

Huang, F., Xu, J., Zeng, Y., Chen, J., Wang, B., Yu, H., Chen, L., Huang, W., and Tan, R., 2017. Slab breakoff of the Neo-Tethys Ocean in the Lhasa Terrane inferred from contemporaneous melting of the mantle and crust. Geochemistry, Geophysics, Geosystems 18, 4074–4095.

Huang, F., Zhang, Z., Xu, J., Li, X., Zeng, Y., Wang, B., Li, X., Xu, R., Fan, Z., and Tian, Y., 2019. Fluid flux in the lithosphere beneath southern Tibet during Neo-Tethyan slab breakoff: Evidence from an appinite–granite suite. Lithos 344, 324–338.

Huang, Y., Zhao, Z.D., Zhang, F.Q., Zhu, D.C., Dong, G.C., Zhou, S. and Mo, X.X., 2010. Geochemistry and implication of the Gangdese batholiths from Renbu and Lhasa areas in southern Gangdese, Tibet: Acta Petrologica Sinica, v. 26, no. 10, p. 3131–3142.

Ji, W.Q., 2010. Geochronology and petrogenesis of granitic rocks from east segment of the Gangdese batholith, southern Tibet: Unpublished result. PhD thesis, Chinese Academy of Sciences.

Ji, W., Wu, F., Chung, S., Li, J., and Liu, C., 2009. Zircon U–Pb geochronology and Hf isotopic constraints on petrogenesis of the Gangdese batholith, southern Tibet. Chem Geol 262, 229–245.

Ji, W., Wu, F., Liu, C., and Chung, S., 2012. Early Eocene crustal thickening in southern Tibet: New age and geochemical constraints from the Gangdese batholith. J Asian Earth Sci 53, 82–95.

Jia, L.L., 2014. Regional variation of geochemical characteristics and tectonic implication of the Early Eocene basic rocks in southern Tibet. MS thesis, China University of Geosciences (Beijing), v., no., p1–64.

Johnson, M.C., and Plank, T., 2000. Dehydration and melting experiments constrain the fate of subducted sediments. Geochem Geophy Geosy 1, 1–26.

Kapp, P., and DeCelles, P.G., 2019. Mesozoic–Cenozoic geological evolution of the Himalayan–Tibetan orogen and working tectonic hypotheses. Am J Sci 319, 159–254.

Kapp, P., DeCelles, P.G., Gehrels, G.E., Heizler, M., and Ding, L., 2007. Geological records of the Lhasa–Qiangtang and Indo–Asian collisions in the Nima area of central Tibet. Geol Soc Am Bull 119, 917–933.

Kapp, P., Murphy, M.A., Yin, A., Harrison, T.M., Ding, L., and Guo, J., 2003. Mesozoic and Cenozoic tectonic evolution of the Shiquanhe area of western Tibet. Tectonics 22, 1–25.

Kearey, P., Klepeis, K.A., and Vine, F.J., 2009. Global Tectonics 3rd (Oxford: John Wiley & Sons) Edition.

King, P.L., White, A., Chappell, B.W., and Allen, C.M., 1997. Characterization and origin of aluminous A-type granites from the Lachlan Fold Belt, southeastern Australia. J Petrol 38, 371–391.

Kinny, P.D., and Maas, R., 2003. Lu–Hf and Sm–Nd isotope systems in zircon. Rev Mineral Geochem 53, 327–341.

Lai, W., Hu, X., Garzanti, E., Xu, Y., Ma, A., and Li, W., 2019. Early Cretaceous sedimentary evolution of the northern Lhasa terrane and the timing of initial Lhasa–Qiangtang collision. Gondwana Res 73, 136–152.

Lee, H., Chung, S., Ji, J., Qian, Q., Gallet, S., Lo, C., Lee, T., and Zhang, Q., 2012. Geochemical and Sr–Nd isotopic constraints on the genesis of the Cenozoic Linzizong volcanic successions, southern Tibet. J Asian Earth Sci 53, 96–114.

Lee, H., Chung, S., Lo, C., Ji, J., Lee, T., Qian, Q., and Zhang, Q., 2009. Eocene Neotethyan slab break-off in southern Tibet inferred from the Linzizong volcanic record. Tectonophysics 477, 20–35.

Lee, T., and Lawver, L.A., 1995. Cenozoic plate reconstruction of Southeast Asia. Tectonophysics 251, 85–138.

Li, X.H., Long, W.G., Li, Q.L., Liu, Y., and Tao, H., 2010. Penglai Zircon Megacrysts: A Potential New Working Reference Material for Microbeam Determination of Hf–O Isotopes and U–Pb Age. Geostandards & Geoanalytical Research 34, 117–134.

Li, H., Wang, M., Zeng, X., Luo, A., and Feng, S., 2021a Zircon U-Pb and Lu-Hf isotopes and geochemistry of granitoids in central Tibet: Bringing the missing Early Jurassic subduction events to light . Gondwana Research 96, 125–146.

Li, S.M., Wang, Q., Zhu, D.C., Cawood, P.A., Stern, R.J., Weinberg, R., Zhao, Z., and Mo, X.X., 2020a. Reconciling Orogenic Drivers for the Evolution of the Bangong-Nujiang Tethys During Middle-Late Jurassic. Tectonics 39, 1–22.

Li, C., Zeng, M., Chen, S., Jin, X., and Cheng, W., 2021 Provenance evolution during passive-to active-margin transition unraveled from an accretionary complex from the Bangong–Nujiang suture zone: Insights into Early Mesozoic Meso-Tethys subduction and source-area tectonics. Gondwana Research 98, 191–211.

Li, C., Zeng, M., Li, Z., and Chen, S., 2020. Origin and tectonic implications of Late Jurassic high-Mg diorites along the Bangong-Nujiang suture zone, Tibet. Int Geol Rev 63, 1406–1422.

Lieu, W.K., and Stern, R.J., 2019. The robustness of Sr/Y and La/Yb as proxies for crust thickness in modern arcs. Geosphere 15, 621–641.

Lin, Y., Zhang, Z., Dong, X., Shen, K., and Lu, X., 2013. Precambrian evolution of the Lhasa terrane, Tibet: Constraint from the zircon U–Pb geochronology of the gneisses. Precambrian Res 237, 64–77.

Liu, Y., Hu, Z., Gao, S., Günther, D., Xu, J., Gao, C., and Chen, H., 2008. In situ analysis of major and trace elements of anhydrous minerals by LA-ICP–MS without applying an internal standard. Chem Geol 257, 34–43.

Liu, Y., Hu, Z., Zong, K., Gao, C., Gao, S., Xu, J., and Chen, H., 2010. Reappraisement and refinement of zircon U-Pb isotope and trace element analyses by LA-ICP–MS. Chinese Science Bulletin 55, 1535–1546.

Liu, Y., Wang, M., Li, C., Li, S., Xie, C., Zeng, X., Dong, Y., and Liu, J., 2019. Late Cretaceous tectono-magmatic activity in the Nize region, central Tibet: Evidence for lithospheric delamination beneath the Qiangtang–Lhasa collision zone. Int Geol Rev 61, 562–583.

Loiselle, M.C., and Wones, D.R., 1979. Characteristics and origin of anorogenic granites. Geol. Soc. Am. 11, 468, Abstracts with Programs.

Ludwig, K.R., 2003. User's manual for isoplot 3.00, a geochronological toolkit for Microsoft excel. Berkeley Geochronl. Cent. Spec. Publ. 4, 25–32.

Lustrino, M., 2005. How the delamination and detachment of lower crust can influence basaltic magmatism. Earth-Sci Rev 72, 21–38.

Ma, X., Xu, Z., and Meert, J.G., 2016. Eocene slab break-off of Neotethys as suggested by dioritic dykes in the Gangdese magmatic belt, southern Tibet. Lithos 248-251, 55–65.

Menuge, J.F., Brewer, T.S., and Seeger, C.M., 2002. Petrogenesis of metaluminous A-type rhyolites from the St Francois Mountains, Missouri and the Mesoproterozoic evolution of the southern Laurentian margin. Precambrian Res 113, 269–291.

Metcalfe, I., 2013. Gondwana dispersion and Asian accretion: Tectonic and palaeogeographic evolution of eastern Tethys. J Asian Earth Sci 66, 1–33.

Miyazaki, K., 2004. Low-P–high-T metamorphism and the role of heat transport by melt migration in the Higo Metamorphic Complex, Kyushu, Japan. J Metamorph Geol 22, 793–809.

Mo, X., Hou, Z., Niu, Y., Dong, G., Qu, X., Zhao, Z., and Yang, Z., 2007. Mantle contributions to crustal thickening during continental collision: Evidence from Cenozoic igneous rocks in southern Tibet. Lithos 96, 225–242.

Mo, X., Niu, Y., Dong, G., Zhao, Z., Hou, Z., Zhou, S., and Ke, S., 2008. Contribution of syncollisional felsic magmatism to

continental crust growth: A case study of the Paleogene Linzizong volcanic Succession in southern Tibet. Chem Geol 250, 49–67.

Motuza, G., and Šliaupa, S., 2017. Paleogene volcanism in Central Afghanistan: Possible far-field effect of the India–Eurasia collision. J Asian Earth Sci 147, 502–515.

Najman, Y., Jenks, D., Godin, L., Boudagher-Fadel, M., Millar, I., Garzanti, E., Horstwood, M., and Bracciali, L., 2017. The Tethyan Himalayan detrital record shows that India–Asia terminal collision occurred by 54 Ma in the Western Himalaya. Earth Planet Sc Lett 459, 301–310.

Niu, Y., Wilson, M., Humphreys, E.R., and O'Hara, M.J., 2011. The Origin of Intra-plate Ocean Island Basalts (OIB): The Lid Effect and its Geodynamic Implications: Journal of Petrology, v. 52, no. 7–8, p. 1443–1468.

Pan, G.T., Ding, J., Yao, D.S., and Wang, L.Q., 2004. Guidebook of 1: 1,500,000 geologic map of the Qinghai-Xizang (Tibet) Plateau and adjacent areas. Chengdu, China: Chengdu Cartographic Publishing House 48.

Replumaz, A., Funiciello, F., Reitano, R., Faccenna, C., and Balon, M., 2016. Asian collisional subduction: A key process driving formation of the Tibetan Plateau. Geology 44, 943–946.

Rudnick, R.L., Gao, S., Holland, H.D., and Turekian, K.K., 2003. Composition of the continental crust. The Crust 3, 1–64.

Schaltegger, U., Zeilinger, G., Frank, M. and Burg, J.P., 2002. Multiple mantle sources during island arc magmatism: U–Pb and Hf isotopic evidence from the Kohistan arc complex, Pakistan: Terra nova, v. 14, no. 6, p. 461–468.

Schiller, D. and Finger, F., 2019. Application of Ti-in-zircon thermometry to granite studies: problems and possible solutions: Contributions to Mineralogy and Petrology, v. 174, no. 6, p. 51. 10.1007/s00410-019-1585-3

Skora, S., Blundy, J.D., Brooker, R.A., Green, E.C., de Hoog, J., and Connolly, J.A., 2015. Hydrous phase relations and trace element partitioning behaviour in calcareous sediments at subduction-zone conditions. J Petrol 56, 953–980.

Song, P.P., Ding, L., Li, Z.Y., Lippert, P.C., and Yue, Y.H., 2017, An early bird from Gondwana: Paleomagnetism of Lower Permian lavas from northern Qiangtang (Tibet) and the geography of the Paleo-Tethys: Earth and Planetary Science Letters, v. 475, p. 119–133.

Stern, R.J., 2002, Subduction zones[J]: Reviews of Geophysics, v. 40, no. 4, p. 1–40.

Sun, S. and McDonough, W.F., 1989. Chemical and isotopic systematics of oceanic basalts: implications for mantle composition and processes: Geological Society, London, Special Publications, v. 42, no. 1, p. 313–345.

Sun, M., Tang, J., Chen, W., Ma, X., Qu, X., Song, Y., Li, X., and Ding, J., 2020. Process of lithospheric delamination beneath the Lhasa–Qiangtang collision orogen: Constraints from the geochronology and geochemistry of Late Cretaceous volcanic rocks in the Lhasa terrane, central Tibet. Lithos 356-357, 105–219.

Tian, Y., Huang, F., Xu, J., Wang, B., Liu, H., Zeng, Y., Liu, X., Yang, C., Yu, H., and Wen, Y., 2021. Neo-Tethyan slab tearing constrained by Palaeocene N-MORB-like magmatism in southern Tibet. Geol J 56, 205–223.

Torsvik, T.H., van der Voo, R., Preeden, U., Mac Niocaill, C., Steinberger, B., Doubrovine, P.V., van Hinsbergen, D.J.J.,

Domeier, M., Gaina, C., Tohver, E., Meert, J.G., McCausland, P.J.A., and Cocks, L.R.M., 2012, Phanerozoic polar wander, palaeogeography and dynamics: Earth Science Reviews 114, p. 325–368.

van Hunen, J., and Allen, M.B., 2011. Continental collision and slab break-off: A comparison of 3-D numerical models with observations: Earth and Planetary Science Letters, v. 302, no. 1–2, p. 27–37.

Viruete, J.E., 1999. One- and two-dimensional thermal modelling of orogenic crustal extension in the Tormes Gneissic Dome, NW Iberian Massif, Spain. International Journal of Earth Sciences 88, 444–457.

Wang, C., Dai, J., Zhao, X., Li, Y., Graham, S.A., He, D., Ran, B., and Meng, J., 2014a. Outward-growth of the Tibetan Plateau during the Cenozoic: A review. Tectonophysics 621, 1–43.

Wang, X.H., Lang, X.H., Tang, J.X., Deng, Y.L., and Cui, Z.W., 2019, Early–Middle Jurassic (182–170 Ma) Ruocuo adakitic porphyries, southern margin of the Lhasa terrane, Tibet: Implications for geodynamic setting and porphyry Cu–Au mineralization: Journal of Asian Earth Sciences, v. 173, p. 336–351.

Wang, C., Liu, Z., and Hébert, R., 2000. The Yarlung–Zangbo paleo-ophiolite, southern Tibet: Implications for the dynamic evolution of the Yarlung–Zangbo Suture Zone. J Asian Earth Sci 18, 651–661.

Wang, R., Richards, J.P., Hou, Z., An, F., and Creaser, R.A., 2015. Zircon U–Pb age and Sr-Nd–Hf–O isotope geochemistry of the Paleocene–Eocene igneous rocks in western Gangdese: Evidence for the timing of Neo-Tethyan slab break-off. Lithos 224-225, 179–194.

Wang, W., Wang, M., Zhai, Q., Xie, C., Hu, P., Li, C., Liu, J., and Luo, A., 2020. Transition from oceanic subduction to continental collision recorded in the Bangong-Nujiang suture zone: Insights from Early Cretaceous magmatic rocks in the north-central Tibet. Gondwana Res 78, 77–91.

Wang, Q., Wyman, D.A., Li, Z., Sun, W., Chung, S., Vasconcelos, P.M., Zhang, Q., Dong, H., Yu, Y., and Pearson, N., 2010. Eocene north-south trending dikes in central Tibet: New constraints on the timing of east-west extension with implications for early Plateau uplift? Earth Planet Sci Lett 298, 205–216.

Wang, Q., Zhu, D., Cawood, P.A., Zhao, Z., Liu, S., Chung, S., Zhang, L., Liu, D., Zheng, Y., and Dai, J., 2015a. Eocene magmatic processes and crustal thickening in southern Tibet: Insights from strongly fractionated ca. 43 Ma granites in the western Gangdese Batholith. Lithos 239, 128–141.

Watson, E.B., and Harrison, T.M., 1983. Zircon saturation revisited: Temperature and composition effects in a variety of crustal magma types. Earth & Planetary Science Letters 64, 295–304.

Watson, E.B., Wark, D.A., and Thomas, J.B., 2006. Crystallization thermometers for zircon and rutile. Contributions to Mineralogy & Petrology 151, 413.

Wen, D., Chung, S., Song, B., Iizuka, Y., Yang, H., Ji, J., Liu, D. and Gallet, S., 2008. Late Cretaceous Gangdese intrusions of adakitic geochemical characteristics, SE Tibet: petrogenesis and tectonic implications: Lithos, v. 105, no. 1–2, p. 1–11. 10.1016/j.lithos.2008.02.005

Whalen, J.B., Currie, K.L., and Chappell, B.W., 1987. A-type granites: Geochemical characteristics, discrimination and petrogenesis. Contrib Mineral Petr 95, 407–419.

Wignall, P.B., 2001. Large igneous provinces and mass extinctions: Earth-science Reviews, v. 53, no. 1–2, p. 1–33.

Wu, F., Liu, X., Ji, W., Wang, J. and Yang, L., 2017. Highly fractionated granites: Recognition and research: Science China Earth Sciences, v. 60, no. 7, p. 1201–1219.

Xu, Y., Lan, J., Yang, Q., Huang, X., and Qiu, H., 2008. Eocene break-off of the Neo-Tethyan slab as inferred from intraplate-type mafic dykes in the Gaoligong orogenic belt, eastern Tibet. Chem Geol 255, 439–453.

Xu, M., Li, C., Zhang, X., and Wu, Y., 2014. Nature and evolution of the Neo-Tethys in central Tibet: Synthesis of ophiolitic petrology, geochemistry, and geochronology. Int Geol Rev 56, 1072–1096.

Yi, J., Wang, Q., Zhu, D., Li, S., Liu, S., Wang, R., Zhang, L., and Zhao, Z., 2018. Westward-younging high-Mg adakitic magmatism in central Tibet: Record of a westward-migrating lithospheric foundering beneath the Lhasa–Qiangtang collision zone during the Late Cretaceous. Lithos 316-317, 92–103.

Yin, A., and Harrison, T.M., 2000. Geologic Evolution of the Himalayan-Tibetan Orogen. Ann. rev.Earth Planet.sci 28, 211–280.

Zeng, Y., Ducea, M.N., Xu, J., Chen, J., and Dong, Y., 2020. Negligible surface uplift following foundering of thickened central Tibetan lower crust. Geology 49, 45–50.

Zeng, Y.C., Xu, J.F., Ducea, M.N., Chen, J.L., Huang, F., and Zhang, L., 2019. Initial Rifting of the Lhasa Terrane from Gondwana: Insights From the Permian (~262 Ma) Amphibole-Rich Lithospheric Mantle-Derived Yawa Basanitic Intrusions in Southern Tibet. Journal of Geophysical Research: Solid Earth 124, 2564–2581.

Zhang, H., Parrish, R., Zhang, L., Xu, W., Yuan, H., Gao, S., and Crowley, Q.G., 2007. A-type granite and adakitic magmatism association in Songpan–Garze fold belt, eastern Tibetan Plateau: Implication for lithospheric delamination. Lithos 97, 323–335.

Zhang, K., Zhang, Y., Tang, X., and Xia, B., 2012. Late Mesozoic tectonic evolution and growth of the Tibetan Plateau prior to the Indo-Asian collision. Earth-Sci Rev 114, 236–249.

Zheng, H., Huang, Q., Kapsiotis, A., Lenaz, D., Velicogna, M., Xu, C., Cheng, C., Xia, B., Liu, W., and Xiao, Y., 2019. Coexistence of MORB-and OIB-like dolerite intrusions in the Purang ultramafic massif, SW Tibet: A paradigm of plume-influenced MOR-type magmatism prior to subduction initiation in the Neo-Tethyan lithospheric mantle. GSA Bulletin 131, 1276–1294.

Zhu, D., Mo, X., Wang, L., Zhao, Z., Niu, Y., Zhou, C., and Yang, Y., 2009. Petrogenesis of highly fractionated I-type granites in the Zayu area of eastern Gangdese, Tibet: Constraints from zircon U-Pb geochronology, geochemistry and Sr-Nd-Hf isotopes. Science in China Series D: Earth Sciences 52, 1223–1239.

Zhu, D., Wang, Q., Chung, S., Cawood, P.A., and Zhao, Z., 2019. Gangdese magmatism in southern Tibet and India–Asia convergence since 120 Ma. Geological Society, London, Special Publications 483, 583–604.

Zhu, D., Zhao, Z., Niu, Y., Dilek, Y., Hou, Z., and Mo, X., 2013. The origin and pre-Cenozoic evolution of the Tibetan Plateau. Gondwana Res 23, 1429–1454.

Zhu, D., Zhao, Z., Niu, Y., Mo, X., Chung, S., Hou, Z., Wang, L., and Wu, F., 2011. The Lhasa Terrane: Record of a microcontinent and its histories of drift and growth. Earth Planet Sc Lett 301, 241–255.

Zong, K., Klemd, R., Yuan, Y., He, Z., Guo, J., Shi, X., Liu, Y., Hu, Z., and Zhang, Z., 2017. The assembly of Rodinia: The correlation of early Neoproterozoic (ca. 900 Ma) high-grade metamorphism and continental arc formation in the southern Beishan Orogen, southern Central Asian Orogenic Belt (CAOB). Precambrian Res 290, 32–48.